

Article

Corrosion Enhancement for FGM Coolant Pipes Subjected to High-Temperature and Hydrostatic Pressure

Kai-Chien Lo * and Hsin-Yi Lai *

Department of Mechanical Engineering, National Cheng Kung University, Tainan 701, Taiwan

* Correspondence: n18051041@gs.ncku.edu.tw (K.-C.L.); hylai@mail.ncku.edu.tw (H.-Y.L.)

Abstract: The objective of this paper is to enhance the corrosion resistance of coolant pipes in high temperature and lateral hydrostatic pressure in critical engineering environment, especially for circular coolant pipes under hydrostatic pressure of LBE (lead-bismuth eutectic) applications in nuclear power plants. The resistance against corrosion caused by LBE liquid is mainly formed by Fe-12Cr-2Si solid solutions coatings on the pipe. The silicon concentration in Fe-12Cr-2Si can interact with LBE as an effective oxidized compound such as SiO_2 and Fe_2SiO_4 when the silicon concentration is higher than 1.25 wt.%. The oxide film formed on the coating can resist the LBE corroding in the Fe-12Cr-2Si structure. The primary material of a constructing coolant pipe is T91 ferritic-martensitic alloys, and the surface anti-corrosion coating is Fe-12Cr-2Si solid solution. With a high strength structure, FGC (functionally graded composite material), ensures that the pipe resists the corrosion from LBE liquid. In this study, both the steady-state stress values and silicon concentration are evaluated at 700, 1000, and 1200 °C to know the fatigue problems. The research result indicates the FGM (functionally graded material) structure performs better in promoting the margin of safety on stress distribution and reserving the silicon concentration on the inner surface higher than 1.25 wt.% over 60 years as compared to the FGC structure with 34 μm thickness of Fe-12Cr-2Si coating in a high temperature environment.



Citation: Lo, K.-C.; Lai, H.-Y. Corrosion Enhancement for FGM Coolant Pipes Subjected to High-Temperature and Hydrostatic Pressure. *Coatings* **2022**, *12*, 666. <https://doi.org/10.3390/coatings12050666>

Academic Editor: Cecilia Bartuli

Received: 1 April 2022

Accepted: 4 May 2022

Published: 13 May 2022

Publisher's Note: MDPI stays neutral with regard to jurisdictional claims in published maps and institutional affiliations.



Copyright: © 2022 by the authors. Licensee MDPI, Basel, Switzerland. This article is an open access article distributed under the terms and conditions of the Creative Commons Attribution (CC BY) license (<https://creativecommons.org/licenses/by/4.0/>).

Keywords: functionally graded material (FGM); functionally graded composite material (FGC); corrosion resistance; lead-bismuth eutectic (LBE)

1. Introduction

Cylindrical shells and tubes conveying fluid are found in numerous industrial applications, particularly in the sections connected with a power generator [1].

Thanks to the advantages of withstanding severe high-temperature gradients while maintaining structural integrity, functionally graded materials (FGMs) have received much more attention in engineering communities, especially in applications for high-temperature environments such as nuclear reactors [1–6].

This study evaluates the structure of nuclear coolant pipes made with FGC and FGM. The traditional FGC structure is made with T91/F91 ferritic-martensitic alloys [7,8]; the LBE liquid is the cooling source for nuclear power [9]. The FGC structure is a component of Fe-Cr-Si solid solutions and ferritic-martensitic alloys like T91/F91. As high strength is required for pipe structures, ferritic-martensitic alloys are the substrate metal of the model when Fe-Cr-Si solid solution is used as the surface corrosion-resisting coating [7–11]. Currently, the working environment temperature of light water reactor (LWR) is about 250 to 700 °C [7–9,11]; the LBE in nuclear coolant pipe is about 250 to 500 °C [12,13]. The Large-Break Loss-of-Coolant Accident (LBLOCA) is considered the worst scenario of nuclear power failure, the temperature could rise to 1200 °C when this accident happened and make the cladding wall fatigue failure [14–16]. Due to the high temperature condition of nuclear power plant, the consideration for thermal stress measurement and corrosion testing is necessary [17–20]. However, the structure for the coolant pipe is constructed

with the Fe-Cr-Si solid solution coating welded on the T91 substrate metal with a thickness of 17~80 μm [7–9]. This composition might make the stress much higher on welding than other places and the silicon concentration lower than 1.25 wt.% because of the large difference of concentration distribution between T91 alloys and Fe-12Cr-2Si. FGM might be an improvement for both strength and corrosion resistance.

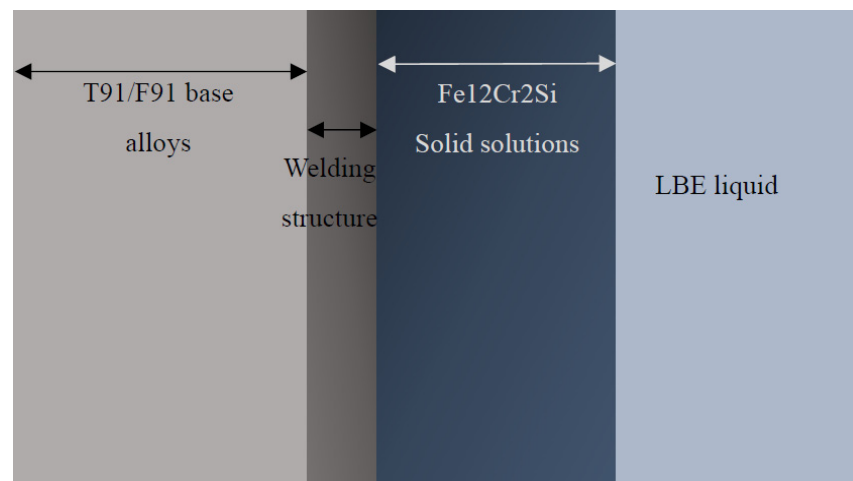
Elliott et al. [8] said the main elements for the corrosion resistance of the Fe-Cr-Si solid solution coating are silicon and chromium, which would remain above the 10.5 wt.% Cr and 1.25 wt.% Si critical concentrations for the respective lifetime of the pipe's material. In this study, the corrosion resistance is demonstrated by the diffusion of silicon concentration; the stress analysis is based on the maximum shear stress theory. Fick's law is the mainly equation for calculating the silicon diffusion from Fe-Cr-Si solutions to the T91 alloy and other material.

Amanda et al. [19] observed the different oxidation process of silicon for the Fe-Cr-Si solid solution has variety of Cr wt.%, which are Fe-12Cr-2Si, Fe-16Cr-2Si and Fe-20Cr-2Si alloys, respectively. In this case, the high concentration of Cr in materials could cause the formation of the protective SiO_2 and Fe_2SiO_4 layers on the pipe surface. This shows that corrosion and oxidation resistance could be improved by transforming the materials. COMSOL Multiphysics 5.4 was used to simulate the diffusion for this research in FGC and FGM. In this study, the TiO_2 is considered the third material used to optimize the FGM structure because of its high strength and low diffusion coefficient [21]. The TiO_2 powder can be combined with other powders in high temperature in the FGM manufacturing process to form the graded distribution [22]. Kim et al. [23] applied laser manufacturing processing to the surface optimized for ATF cladding, the graded structure formed on the surface consisted of Fe-Cr coatings and the based material Zircaloy-4. This processing can be applied on the graded material manufacturing and experiments in this research.

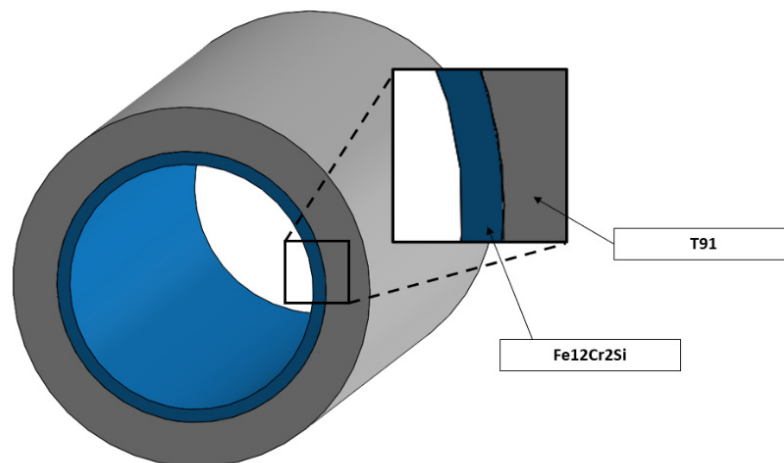
Zhang et al. [24] applied laser additive manufacturing (AM) techniques to form a uniform FGM structure without casting, this would allow a lower budget for FGM forming; therefore, the 3D laser printing technique can be applied to create the FGM coolant pipe without casting molds.

The coolant pipes used in this research, have an inner diameter of 3.81 cm and outer diameter of 4.83 cm [7]; The length of a coolant pipe nowadays varies from 0.94 to 5.7 m [8]; because of the high remarkable difference between lengths and diameters, the 2D plane strain modeling is used as the circular model for the pipes. Ronald et al. [7] analyzed the diffusion of silicon concentration within different thickness of Fe-12Cr-2Si coating on the F91 substrate, this model is shown in Figure 1. The inner surface contacting with the LBE could keep the silicon concentration at a level higher than 1.25 wt.% for 60 years within a welding thickness of 34 μm of Fe-12Cr-2Si coating when the environmental temperature is 700 °C. The diffusion and mechanical behaviors are evaluated for the FGC and FGM structures applied to pipe designing.

This paper proposes a novel FGM model which has a higher margin of safety calculated by the maximum shear stress theory, the silicon concentration on the inner pipe's surface contacting with the LBE liquid can be maintained higher than 1.25 wt.% over 60 years in a high temperature like 1000 °C environments. However, the margin of safety from traditional FGC model is rarely evaluated. In 2018, Kwangwon and Kyohun applied SiC and Zry-4 alloys as the based material of nuclear reactor fuel cladding, the highest margin of safety is range from 76% to 98% when the fuel cladding is made by SiC [14]. The margin of safety of FGM will be analyzed in Section 4 and compared with the SiC structure.



(a)



(b)

Figure 1. (a). Nuclear reactor coolant system (b). Pipe structure.

2. FGMs and Material-Property Estimation Approaches

Nowadays, the research of coolant pipes applied in nuclear power plants focuses on corrosion and oxidation resistance [7–9,18,20]; however, the traditional welding structure of FGC may cause stress concentration and shorten the life of the system. In this study, Fick's law for diffusion equation is applied to the silicon concentration evaluation of Fe-12Cr-2Si films; stress distribution from the LBE hydrostatic pressure is evaluated for high-temperature environments at 700, 1000 and 1200 °C.

The FGM mixture is based on the linear rule of mixture method [25–27]; the volume mixture for two-phase materials can be described as below,

$$\begin{aligned} V_m(y) &= [(d_G - y)/2d_G]^N \\ V_c(y) &= 1 - V_m(y) \end{aligned} \quad (1)$$

V_m : First-phase volume fraction, V_c : second-phase volume fraction, d_G : distance, N : non-negative real numbers. Accordingly, the initial concentration and diffusion coefficient can be taken as [25,26],

$$\begin{aligned} C(x) &= V_m C_m + V_c C_c \\ D(x) &= V_m D_m + V_c D_c \end{aligned} \quad (2)$$

The thermomechanical properties of dual-phase FGM have been estimated through several approaches; Cho et al. [28] calculated the linear rule of the mixture and the Wakashima-Tsukamoto estimate compared to the discretized model, which indicates that the accuracy of the second numerical method is higher than the first approach. According to the Wakashima-Tsukamoto estimate, the averaged bulk modulus K , shear modulus μ , elastic modulus E , Poisson's ratio ν and thermal expansion coefficient α are computed by,

$$K = K_m + \frac{aV_c K_m (K_c - K_m)}{V_m K_c + aV_c K_m} \quad (3)$$

$$\mu = \mu_m + \frac{bV_c \mu_m (\mu_c - \mu_m)}{V_m \mu_c + bV_c \mu_m} \quad (4)$$

$$E = 9K\mu / (3K + \mu) \quad (5)$$

$$\nu = (3K - 2\mu) / [2(3K + \mu)] \quad (6)$$

$$\alpha = \alpha_m + \frac{(1/K - 1/K_m)(\alpha_c - \alpha_m)}{1/K_c - 1/K_m} \quad (7)$$

$$a = K_c(3K_m + 4\mu_m) / K_m(3K + 4\mu_c) \quad (8)$$

$$b = \mu_c(1 + e) / (\mu_m + e\mu_c) \quad (9)$$

$$e = (9K_m + 8\mu_m) / (6K_m + 12\mu_m) \quad (10)$$

In this research, Fe-12Cr-2Si, T91 alloys, and TiO₂ are the essential materials for the FGM structure. The design of FGM is based on the FGC structure, which consists of Fe-12Cr-2Si and T91 alloys; the FGM is classified as a two-phase FGM or three-phase FGM. The two-phase material is Fe-12Cr-2Si-T91, which varies from Fe-12Cr-2Si to T91 continuously. The three-phase material varies from Fe-12Cr-2Si to TiO₂; then TiO₂ turns into T91 gradually; these processes can be depicted by Equation (1).

The physical properties of Fe-12Cr-2Si, TiO₂, T91 alloys, and LBE are listed in Table 1. The elastic modulus of T91 alloys changes with the temperature; the variation between elastic modulus and temperature can be depicted as follows [29],

$$\begin{aligned} E [\text{Mpa}] &= 207300 - 64.58T [^\circ\text{C}] \quad 20^\circ\text{C} \leq T \leq 500^\circ\text{C} \\ E [\text{Mpa}] &= 295000 - 240T [^\circ\text{C}] \quad 500^\circ\text{C} \leq T \end{aligned} \quad (11)$$

Table 1. Mechanical properties [20,30–33].

	Elastic Modulus	Poisson Ratio	Thermal Expansion	Bulk Modulus
Fe12Cr2Si	216.4 (GPa)	0.31	5.2×10^{-5} (1/K)	1.89×10^{11}
T91	-	0.27	1.3×10^{-5} (1/K)	1.73×10^{11}
TiO ₂	230 (GPa)	0.27	9×10^{-6} (1/K)	1.67×10^{11}
LBE	92.8 (MPa)	0.4995	1.285×10^{-4} (1/K)	3.093×10^{10}

3. Construction and Assumptions for FGM Coolant Pipes

3.1. Safety Margin Analysis and Maximum Shear Stress Theory

Kwangwon. et al. [14] analyzed the stress distribution of nuclear power cladding based on the temperature variation during a significant break loss-of-coolant accident and calculated the margin of safety in Equation (13). The conclusion shows that the SiC can increase the cladding's margin of safety by 15.68–16.14% compared to Zry-4. The highest margin of safety is about 95–98% based on this result. The margin of safety for the coolant

pipe in this study is evaluated to ensure that the value is higher than 98%; both safety factors and margin of safety are depicted as follows [34],

$$\text{Safety factor} = \text{F.S.} = \text{ultimate load} / \text{allowable load} \quad (12)$$

$$\text{Margin of safety} = \text{M.O.S.} = \text{F.S.} - 1.0 \quad (13)$$

According to the maximum shear stress theory, it could be used for the evaluation of cladding strength [14],

$$\tau_{\max} = \max(|\sigma_1 - \sigma_2|, |\sigma_1 - \sigma_3|, |\sigma_2 - \sigma_3|) \quad (14)$$

σ_1 , σ_2 and σ_3 are the three maximum principal stresses of the circular model respectively. In this research, the maximum shear stress should be lower than half of the yield strength and the margin of safety must be higher than 95–98%.

3.2. The Thermal Stress Boundary Condition of Coolant Pipes

According to recent studies about corrosion tests on coolant pipes, the oxidation on the pipe surface expands due to the tremendous amount of tensile stress and shear stress when LBE imposes the hydrostatic pressure on it. The higher shear stress caused by the turbulence from LBE on the pipe's surface may also increase corrosion invasion [10,13,35–37].

In this study, the hydrostatic pressure level is based on temperature changes [31]. This pressure from LBE can be described as,

$$P = K_{LBE} \alpha_{LBE} \Delta T \quad (15)$$

α_{LBE} , K_{LBE} are described as thermal expansion and bulk modulus for LBE respectively. The force equilibrium in the radial direction is based on Kwangwon et al. [14],

$$\frac{d\sigma_{rr}}{dr} + \frac{\sigma_{rr} - \sigma_{\theta\theta}}{r} = 0 \quad (16)$$

Hook's law,

$$\varepsilon_{rr}^e = \frac{1}{E} [\sigma_{rr} - \nu(\sigma_{\theta\theta} + \sigma_{zz})] \quad (17)$$

$$\varepsilon_{\theta\theta}^e = \frac{1}{E} [\sigma_{\theta\theta} - \nu(\sigma_{rr} + \sigma_{zz})] \quad (18)$$

$$\varepsilon_{zz}^e = \frac{1}{E} [\sigma_{zz} - \nu(\sigma_{\theta\theta} + \sigma_{rr})] \quad (19)$$

Strain-displacement relationships for plane strain condition,

$$\varepsilon_{\theta\theta}^e = \frac{u}{r} - \alpha \Delta T \quad (20)$$

$$\varepsilon_{rr}^e = \frac{\partial u}{\partial r} - \alpha \Delta T \quad (21)$$

$$\varepsilon_{zz}^e = -\alpha \Delta T \quad (22)$$

where σ_{rr} and $\sigma_{\theta\theta}$ are the radial and hoop stress components respectively; for the thick hollow cylinder, σ_{rr} and $\sigma_{\theta\theta}$ are given in terms of the radial displacement u by,

$$\sigma_{rr} = \left[A_{11} \frac{\partial u}{\partial r} + A_{12} \frac{u}{r} + A_{13} \alpha \Delta T \right] \cdot E \quad (23)$$

$$\sigma_{\theta\theta} = \left[A_{12} \frac{\partial u}{\partial r} + A_{11} \frac{u}{r} + A_{13} \alpha \Delta T \right] \cdot E \quad (24)$$

$$\sigma_{zz} = -\alpha \Delta T \cdot E + \nu(\sigma_{rr} + \sigma_{\theta\theta}) \quad (25)$$

For plane strain condition, E is the modulus of elasticity and A_{11} , A_{12} and A_{13} are related to Poisson’s ratio ν as,

$$A_{11} = \frac{1 - \nu}{(1 + \nu)(1 - 2\nu)} \tag{26}$$

$$A_{12} = \frac{\nu}{(1 + \nu)(1 - 2\nu)} \tag{27}$$

$$A_{13} = \frac{-1}{1 - 2\nu} \tag{28}$$

The substitution of Equations (26)–(28) for Equation (16) produces the Navier equation,

$$\frac{\partial^2 u}{\partial r^2} + \left(\frac{1}{E} \frac{\partial E}{\partial r} + \frac{1}{r}\right) \frac{\partial u}{\partial r} + \left(\frac{A_{12}}{A_{11} E \cdot r} \cdot \frac{\partial E}{\partial r} - \frac{1}{r^2}\right) u = -\frac{A_{13}}{A_{11} E} \frac{\partial(E \cdot \alpha \Delta T)}{\partial r} \tag{29}$$

For the hollow cylinder submitted to uniform hydrostatic pressures P from Equation (15) on the inner surfaces, the mechanical boundary conditions can be expressed as,

$$\sigma_{rr}|_{r=38.1/2} = P, \quad \sigma_{rr}|_{r=48.3/2} = 0 \tag{30}$$

A schematic of the 2D plane strain part with the hydrostatic pressure boundary conditions is shown in Figure 2.

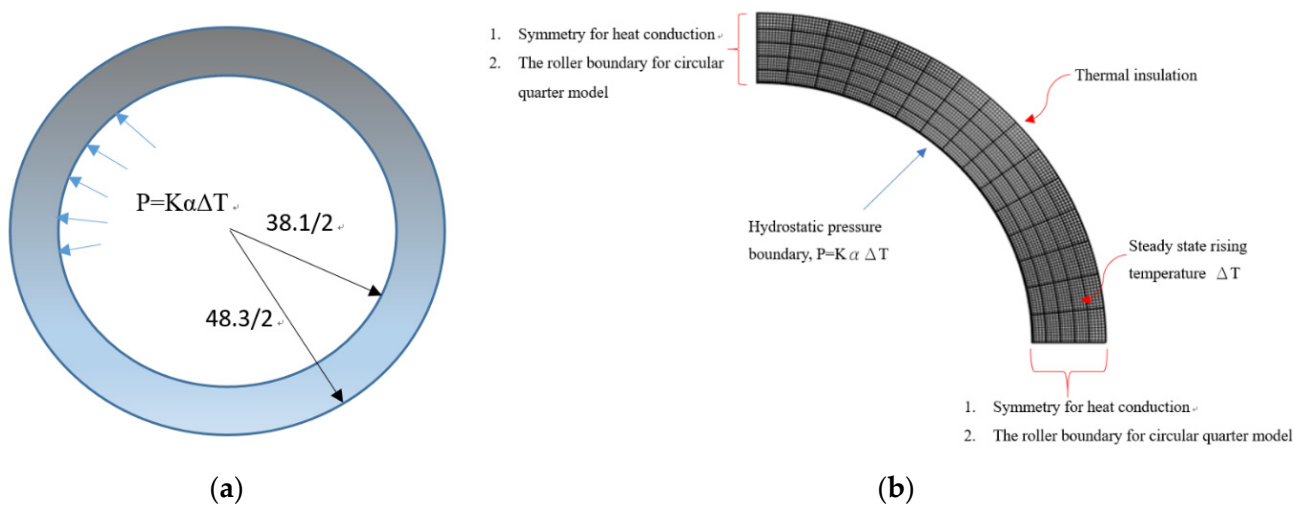


Figure 2. (a) Schematic of 2D circular pipe with the pressure boundary condition. (b) Schematic of 2D circular quarter model in COMSOL 5.4 with the pressure and thermal boundary condition.

Since $(\sigma_{rr}, \sigma_{\theta\theta}, \sigma_{zz})$ are the primary principal stresses, the maximum shear stress theory is depicted by Equation (14),

$$\tau_{\max} = \max(|\sigma_{rr} - \sigma_{\theta\theta}|, |\sigma_{rr} - \sigma_{zz}|, |\sigma_{\theta\theta} - \sigma_{zz}|) \tag{31}$$

The mesh element for the circular model is an eight-node quadrilateral element. There are two translational degrees of freedom at each node, viz., radial displacement u and circumferential displacement v . In the analysis, the circumferential displacement vanishes. This implies that the rotation in the circumferential direction is constrained, but the cylinder is free to expand axially and radially. The schematic is shown in Figure 2a. the finite element model is quarter for the entire circular model as shown in Figure 2b.

3.3. Tamura-Tomota-Ozawa (TTO) Model

The TTO model assumes that the magnitude of stress and strain on every area of two-phase FGM material is dependent on stress and strain of phase constituents undergone with their volume fractions as given [38,39],

$$\begin{aligned}\sigma &= \sigma_1 V_1 + \sigma_2 V_2 \\ \varepsilon &= \varepsilon_1 V_1 + \varepsilon_2 V_2\end{aligned}\quad (32)$$

where σ and ε represent the stresses and strains on every region of a two-phase FGM with various volume fractions of V_1 and V_2 , this model can determine the yield strength of FGMs as given in Equation (1), such as elastic modulus and thermal expansion coefficient,

$$\sigma_y = \sigma_{y1} \left[V_1 + \left(\frac{q + E_1}{q + E_2} \right) \left(\frac{E_2}{E_1} \right) (1 - V_1) \right] \quad (33)$$

σ_{y1} is the yield strength of phase 1 material. Here q indicates the stress to strain ratio that depends on material types and micro-structural interactions among the two phases. It is calculated based on the distribution of the yield strength of two-phase conditions like Figure 3.

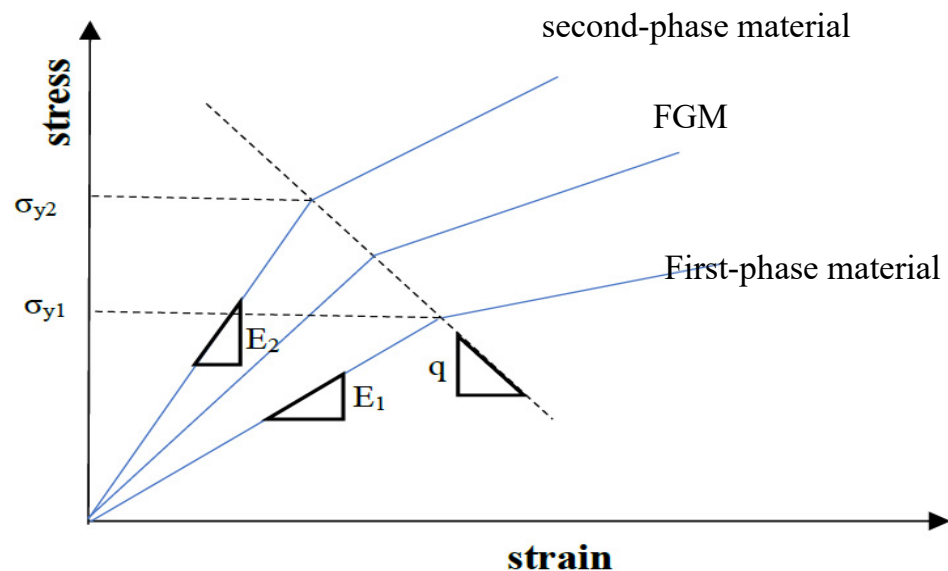


Figure 3. The stress vs. strain curve of an arbitrary two-phase FGM (E_1 : First-phase material, E_2 : Second-phase material).

According to the yield strength-temperature relation of T91 alloys and Fe-12Cr-2Si solid solutions [8], the yield strength at different temperatures varying from 700 to 1200 °C is calculated through the curve fitting of the data from the tensile strength experiment; the yield strength of dioxide titanium is provided by the AZO [32]; which is 333.3 MPa.

3.4. The Diffusion Boundary Conditions for the Evaluation of Corrosion Testing

The silicon concentration moves from regions of high concentrations to regions of low concentrations at a rate proportional to the concentration gradient. Fick's law was applied to depict this diffusive flux in multiple dimensions mathematically [40],

$$\frac{\partial c}{\partial t} = \nabla \cdot (D \nabla \cdot c) \quad (34)$$

$c(x, t)$ is the concentration function which varies based on different regions and time steps; D (m^2/s) is the diffusion coefficient, which is described as an Arrhenius-based diffusion coefficient [8],

$$D = D_0 \exp(-E_A/RT) \left[\frac{\text{m}^2}{\text{s}} \right] \quad (35)$$

where D_0 is the temperature-independent diffusion constant, E_A is the activation energy of the process in J/mol, R is the universal gas constant (8.314 J/mol-K), and T is the absolute temperature in Kelvin. Ballinger et al. [8] wrote the program of minimum mean squared error (MSE) in C to fit the diffusion coefficient for silicon in BCC T91/F91 alloys,

$$D_{si \text{ in } bcc \text{ T91}} = 5 \times 10^{-3} \exp(-253969/RT) \text{ [m}^2/\text{s]} \quad (36)$$

The silicon diffusion coefficient in Fe-12Cr-2Si can be roughly estimated through $D_{si} = 10^{-14} \text{ m}^2/\text{s}$ at high temperatures in the Fe-12Cr-2Si/Cr interfacial region aged experiment [20]. The diffusion of silicon in titanium dioxide, which has 10% oxygen content, can also be expressed by an Arrhenius equation; the diffusion coefficient can be evaluated through a linear function for temperatures above 300 °C [21],

$$D_{si \text{ in } \text{TiO}_2} = 2.43 \times 10^{-18} \exp(-15000/RT) \text{ [m}^2/\text{s]} \quad (37)$$

In this research, the 2D finite element model is tubular cross-sections; the cylindrical coordinates (r, θ) , the diffusion process of Equation (34) is described by the classical diffusion equation for cylindrical coordinates,

$$\frac{\partial c}{\partial t} = \frac{1}{r} \left(\frac{\partial}{\partial r} \left(r \cdot D \frac{\partial c}{\partial r} \right) + \frac{\partial}{\partial \theta} \left(\frac{D}{r} \frac{\partial c}{\partial \theta} \right) \right) \quad (38)$$

When the LBE goes through the inner wall of the coolant pipe, the silicon diffusion coefficient of LBE can be estimated by first principles molecular dynamics (FPMD), which is about $3.8 \times 10^{-5} \text{ m}^2/\text{s}$. this system can be performed in a pure LBE systems to evaluate the diffusion coefficient of silicon atoms [41].

The Finite element approach using a two-dimensional transient problem has been developed with Equation (38) to analyze the diffusion condition of the FGM and FGC structures in the 700, 1000 and 1200 °C environments.

3.5. Modeling Procedure

The research steps for coolant pipe designing can be depicted as follows,

1. Structure designing for the FGC structure, two-phase FGM structure (Fe-12Cr-2Si-T91), and three-phase FGM structure (Fe-12Cr-2Si-TiO₂-T91).
2. Steady-state analysis for stress distribution from the hydrostatic pressure boundary of LBE and high-temperature environments.
3. The designing of corrosion resistance from LBE to the inner wall of coolant pipes.

In this study, the margin of safety shows the strength of the coolant pipes; the silicon concentration should be considered too. The diffusion coefficient of TiO₂, which is very low, may ensure that the three-phase FGM (Fe-12Cr-2Si-TiO₂-T91) reduces the diffusion of surface silicon concentration compared to the two-phase model (Fe-12Cr-2Si-T91). Both of two-phase and three-phase model are evaluated for the margin of safety and the diffusion problem as shown in Figure 4. In this study, the main targets can be illustrated with Table 2. The margin of safety must be higher than 98%; the silicon concentration should be maintained higher than 1.25 wt.% in a high temperature environment.

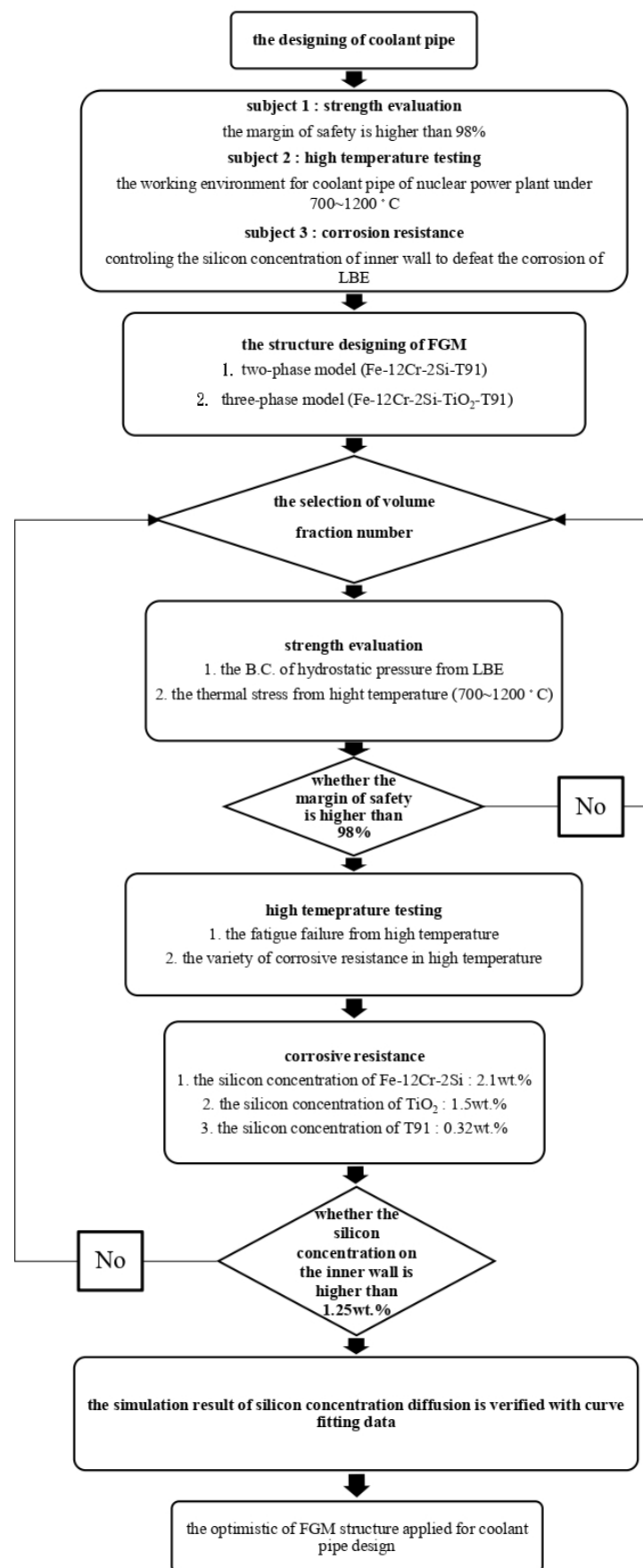


Figure 4. Plate analysis of FGM/FGC coolant pipes.

Table 2. The research targets.

	700 °C	1000 °C	1200 °C
High-Strength (margin of safety)	≥98%	≥98%	≥98%
High-temperature resistance (wt.%)	-	≥1.25 wt.%	≥1.25 wt.%
Corrosion testing (wt.%)	≥1.25 wt.%	-	-

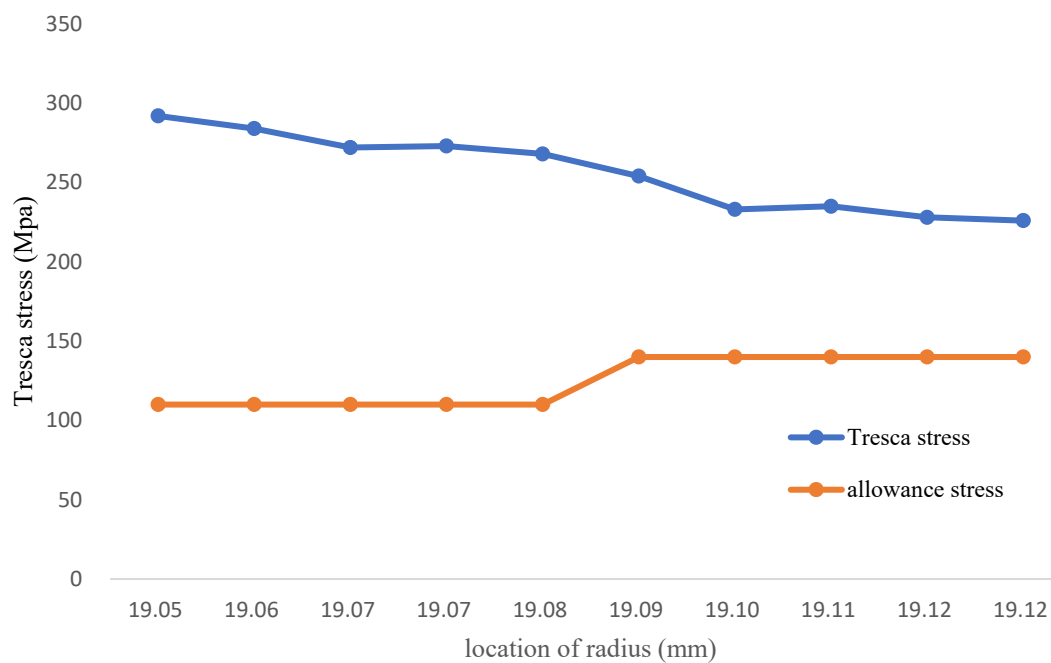
4. Simulation Analysis and Discussion

4.1. FGC Structure Analysis

In this study, the FGC coolant pipe is created by welding Fe-12Cr-2Si solid solutions with a thickness of 34 μm on the T91/F91 circular structure; the margin of safety for the FGC analysis should be higher than 98%. However, Figure 5a and Table 3 shows that when dividing the yield strength between the layer of 0 and 80 μm close to the inner wall of the coolant pipe by 98% in a 700 °C environment, the tresca stress distribution is significantly higher than the allowance stress. Especially the tresca stress of the inner wall, which is higher than twice of the allowance stress.

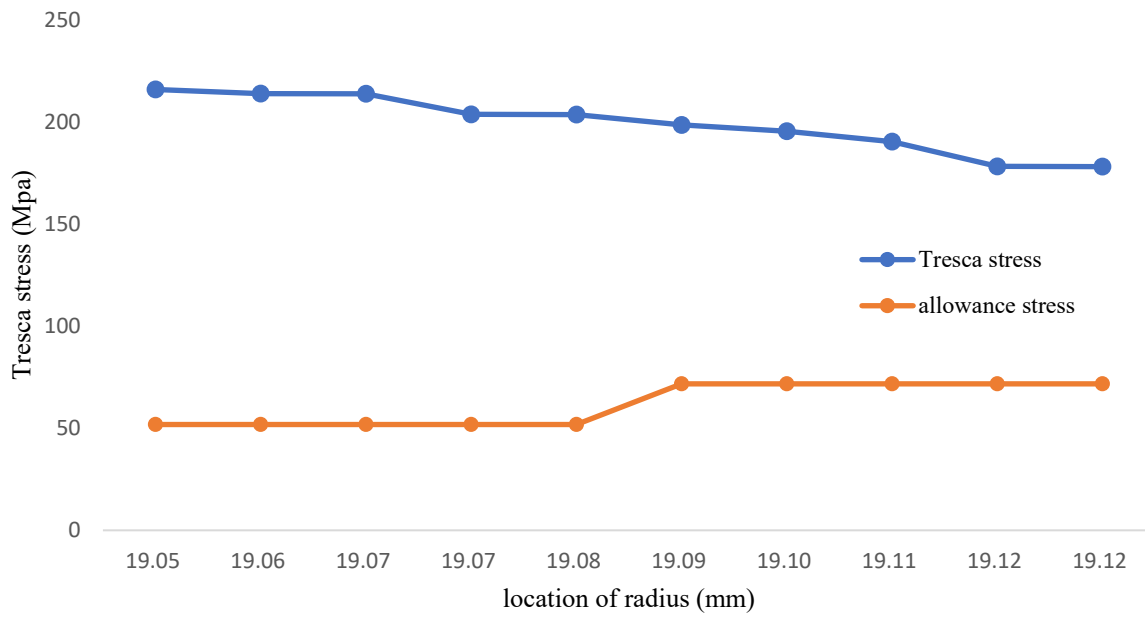
Table 3. The tresca stress and allowance strength (FGC, Temperature: 700 °C).

Location (mm)	19.05	19.05	19.06	19.07	19.08	19.09	19.09	19.10	19.11	19.12
Allowance	110.0	110.0	110.0	110.0	110.0	140.0	140.0	140.0	140.0	140.0
Tresca stress	292.00	284.00	272.00	273.00	268.00	254.00	233.00	235.00	228.00	226.00

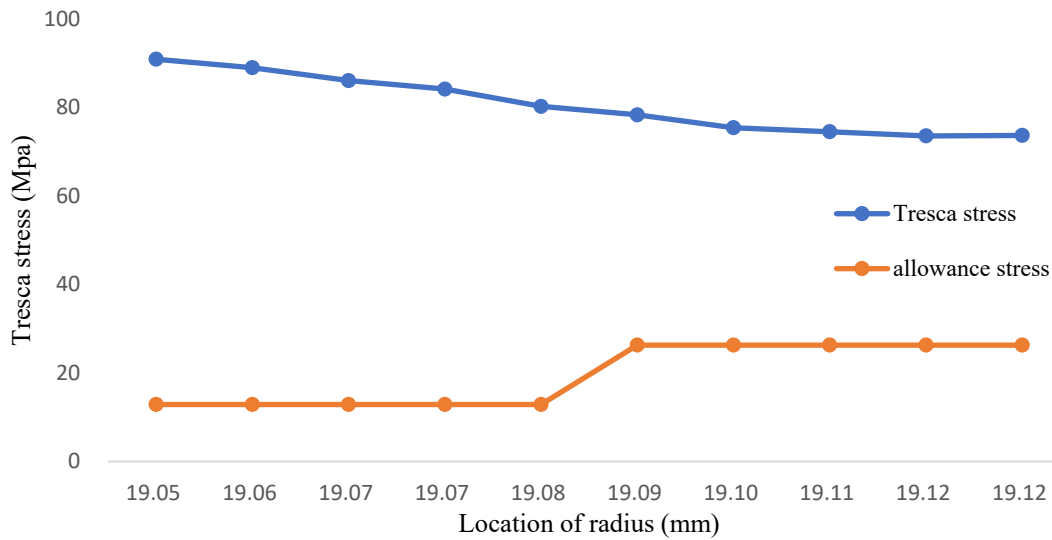


(a)

Figure 5. Cont.



(b)



(c)

Figure 5. (a) The Tresca stress of FGC structure (Temperature: 700 °C); (b) FGC structure Tresca stress (Temperature: 1000 °C); (c) FGC structure Tresca stress (Temperature: 1200 °C).

When the environment temperature rises to 1000 °C, the allowance stress becomes lower because the yield strength declined. However, the tresca stress on the inner wall is higher than four times of allowance stress as shown in Figure 5b and Table 4. The tresca stress will be higher than yield strength which makes the coolant pipe model into plastic deformation. When the temperature is 1200 °C, the allowance stress is range from 12.9~26.30 Mpa; even though the tresca stress is reduced comparatively. The tresca stress is higher than yield strength and make the coolant pipe model into plastic deformation, as shown in Figure 5c and Table 5. All the results indicate the FGC structure applied on coolant pipe are at the risk of plastic deformation and fracture occurs.

Table 4. The tresca stress and allowance strength (FGC, Temperature: 1000 °C).

Location (mm)	19.05	19.05	19.06	19.07	19.08	19.09	19.09	19.10	19.11	19.12
Allowance	51.76	51.76	51.76	51.76	51.76	71.65	71.65	71.65	71.65	71.65
Tresca stress	215.84	213.76	213.68	203.59	203.50	198.41	195.33	190.24	178.15	178.07

Table 5. Tresca stress and allowable strength (FGC, Temperature: 1200 °C).

Location (mm)	19.05	19.05	19.06	19.07	19.08	19.09	19.09	19.10	19.11	19.12
Allowance	12.90	12.90	12.90	12.90	12.90	26.30	26.30	26.30	26.30	26.30
Tresca stress	90.90	88.09	86.07	84.16	80.25	78.34	75.42	74.51	73.60	73.68

The silicon concentration of Fe-12Cr-2Si is 2.11 wt.% when that of T91 alloys is only 0.32 wt.%. However, the traditional welding FGC structure might lower the surface concentration to less than 1.25 wt.% when the inner wall contacts the LBE liquid [7].

Fick's law in Equation (38) is used in the diffusion analysis of silicon concentration. 1.25 wt.% is standard for the corrosion resistance of the inner wall; the distance between the location of 1.25 wt.% and the inner wall is shown in Figure 6 and Table 6; the figure illustrates the location-time relation of the diffusion when the temperature environment is 700 °C. The simulation result is compared with the curve fitting made by analyzing the diffusion of T91/F91 in the semi-infinite region [7], which is shown as Equation (34). The simulation shows that the 1.25 wt.% concentration arrives at the 34 µm location after 6.7×10^5 h, meaning the corrosion resistance of Fe-12Cr-2Si on the T91/F91 circular model lasts for about 60 years. The simulation process has considered the LBE diffusion boundary; therefore, the result is more accurate than the curve fitting condition.

$$y = -40.4867 + 5.60517 \cdot \ln(x + 1353.52) \quad (39)$$

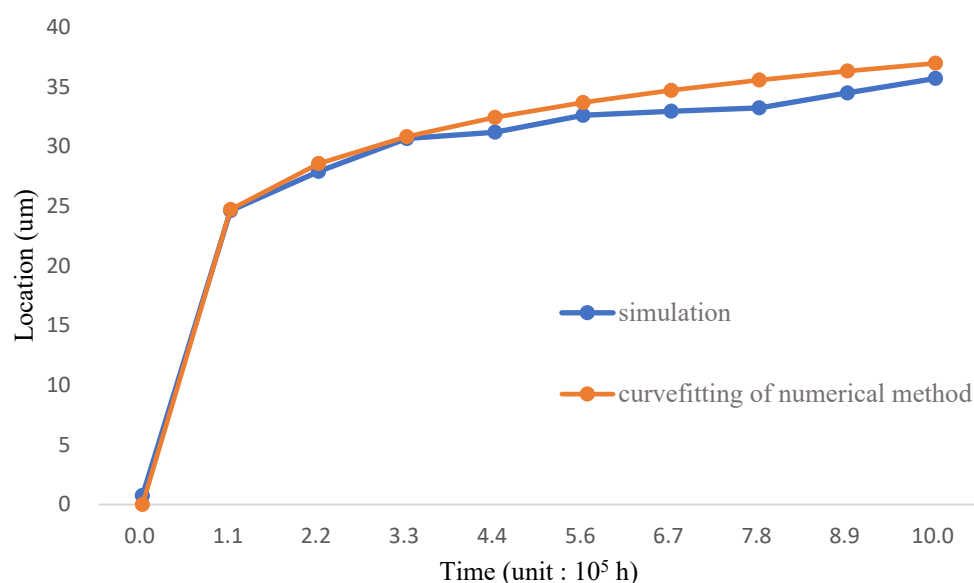
**Figure 6.** The Corrosion levels as compared to FGC location of 1.25 wt.% against time distribution (Temp: 700 °C) [7].

Table 6. FGC the location of 1.25 wt.%—time relation (Temperature: 700 °C).

Time (10 ⁵ h)	0.00	1.11	2.23	3.34	4.45	5.57	6.66	7.78	8.89	10.00
simulation	0.758	24.613	27.898	30.651	31.184	32.598	32.936	33.224	34.470	35.688
Curve-fitting	0.00	24.70	28.56	30.82	32.42	33.67	34.69	35.55	36.30	36.96

As shown in Figure 6, the Fe-12Cr-2Si coating has no corrosion resistance after 6.7×10^5 h; the concentration of the inner wall is evaluated at 700, 1000 and 1200 °C, respectively in Figure 7 and Table 7. The diffusion under the 700 °C environment is the same as in Figure 6. However, the concentration of the FGC structure drops drastically before the end of 9×10^4 h when the temperature is higher than 1000 °C. Therefore, the FGC structure should be optimized because of the strength design and the corrosion problems.

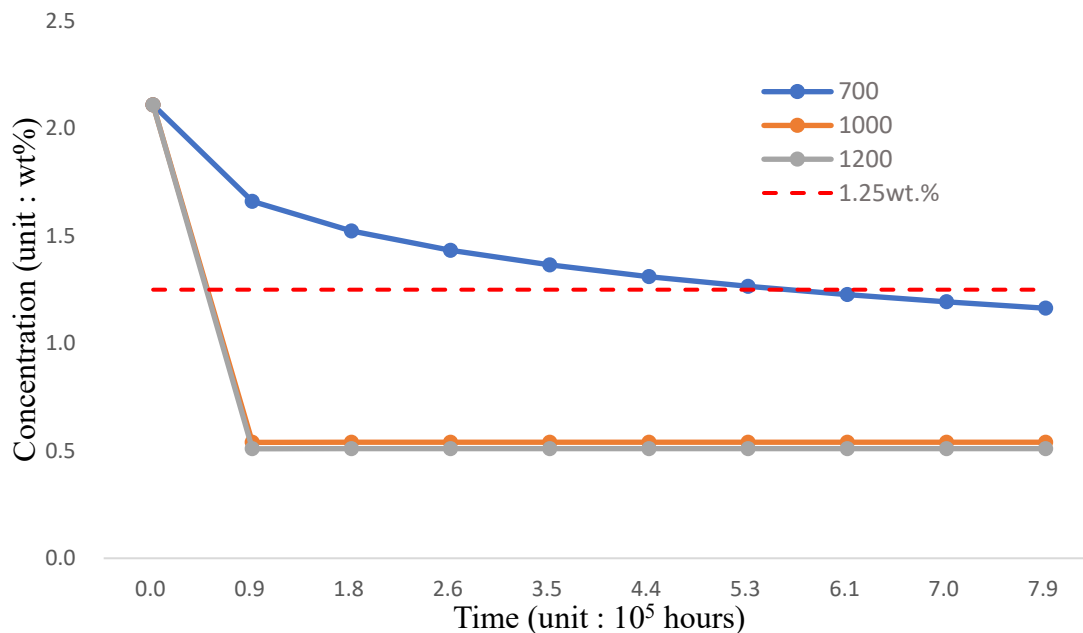


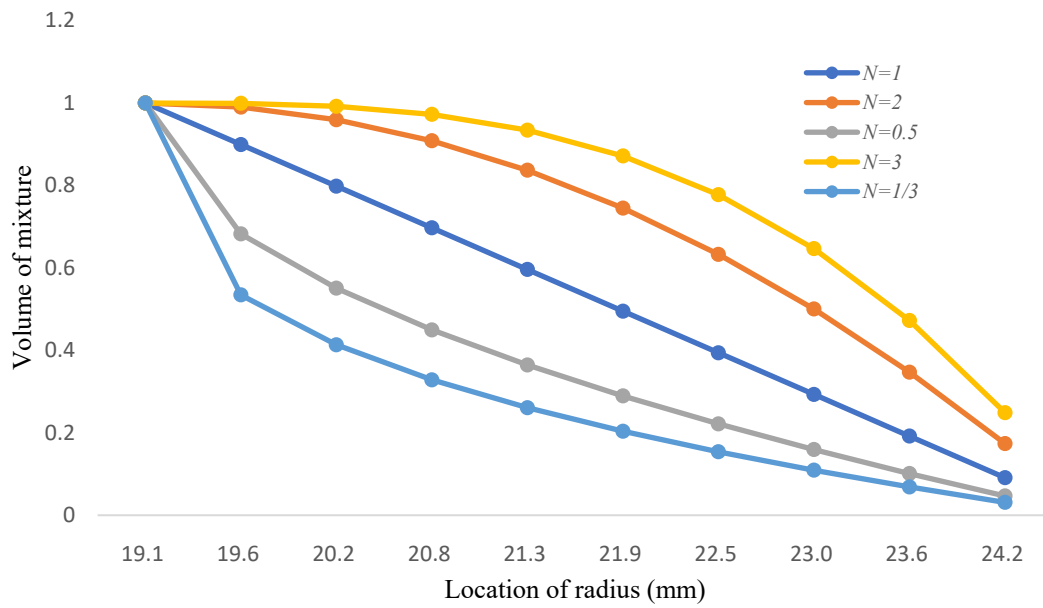
Figure 7. FGC concentration-time distribution.

Table 7. FGC concentration-time distribution.

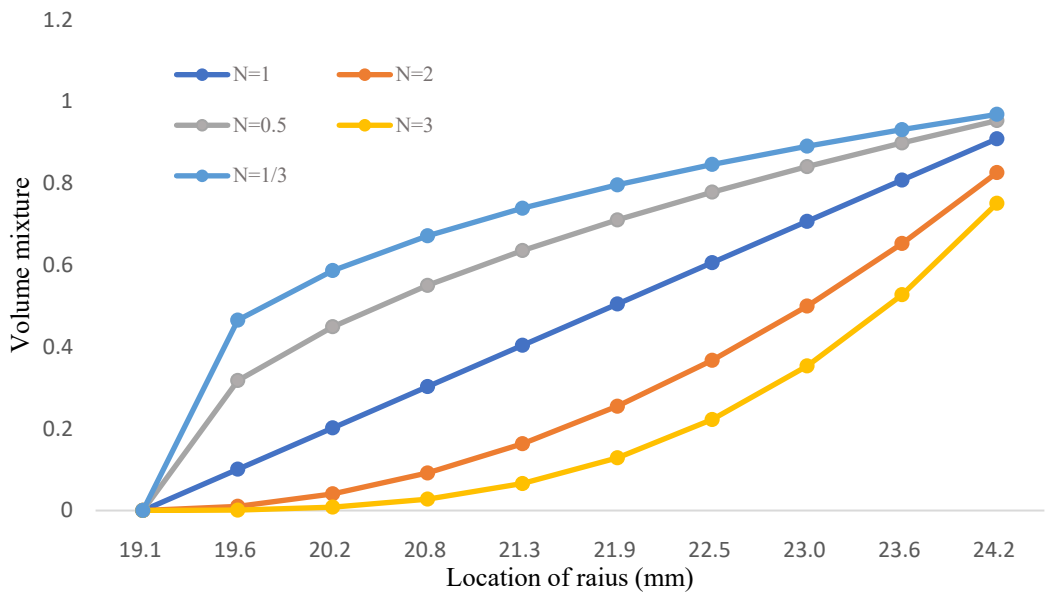
Time (10 ⁵ h)	0.00	0.87	1.75	2.62	3.50	4.38	5.25	6.13	7.00	7.88
T = 700 °C	2.101	1.661	1.523	1.432	1.364	1.310	1.265	1.226	1.193	1.163
T = 1000 °C	2.101	0.539	0.538	0.538	0.538	0.538	0.538	0.538	0.538	0.538
T = 1200 °C	2.101	0.509	0.508	0.508	0.508	0.498	0.498	0.498	0.498	0.498

4.2. Characterization of Structural for Two-Phase FGM Pipes (Fe-12Cr-2Si-T91)

The FGM structure might be a solution for the FGC defects nowadays because of its continuous distribution of materials. The typical FGM is based on the linear rule of mixture designs [28,39]; the two-phase FGM model consists of Fe-12Cr-2Si solid solutions and T91 alloys. The exponential number of volume mixture is 1, 2, 3, 1/2 and 1/3; these numbers show the increasing and decreasing trend of FGM in Figure 8.



(a)



(b)

Figure 8. (a) The volume mixture of Fe-12Cr-2Si for two-phase FGM; (b) The volume mixture of T91 for two-phase FGM.

The volume mixture of Fe-12Cr-2Si is presented in Figure 8a and Table 8. The ratio of Fe-12Cr-2Si decreases gradually and turns into T91 alloys; the volume mixture of T91 alloys is shown in Figure 8b and Table 9, the distribution of the two-phase model is influenced by the variation of volume fraction number from Fe-12Cr-2Si. The volume mixture of T91 is one minus the fraction number of Fe-12Cr-2Si.

Table 8. The volume mixture of Fe-12Cr-2Si for two-phase FGM.

Location (mm)	19.05	19.61	20.18	20.75	21.31	21.88	22.45	23.01	23.58	24.15
$N = 1$	1	0.889	0.778	0.667	0.556	0.444	0.333	0.222	0.199	0.090
$N = 2$	1	0.984	0.950	0.889	0.809	0.698	0.556	0.306	0.347	0.175
$N = 3$	1	0.993	0.958	0.985	0.988	0.948	0.863	0.712	0.473	0.246
$N = 1/2$	1	0.667	0.595	0.465	0.333	0.254	0.183	0.113	0.101	0.046
$N = 1/3$	1	0.306	0.286	0.198	0.1497	0.119	0.072	0.041	0.068	0.031

Table 9. The volume mixture of T91 for two-phase FGM.

Location (mm)	19.05	19.61	20.18	20.75	21.31	21.88	22.45	23.01	23.58	24.15
$N = 1$	0	0.111	0.222	0.333	0.444	0.556	0.667	0.778	0.889	0.909
$N = 2$	0	0.012	0.043	0.111	0.191	0.302	0.444	0.608	0.713	0.826
$N = 3$	0	0.008	0.027	0.065	0.128	0.226	0.353	0.527	0.751	0.758
$N = 1/2$	0	0.333	0.475	0.575	0.667	0.756	0.897	0.887	0.949	0.953
$N = 1/3$	0	0.465	0.586	0.671	0.739	0.796	0.928	0.846	0.890	0.968

In this study, the allowance strength of the two-phase FGM is calculated by converting the yield strength and volume fraction of Equations (33) and (32), the yield strength is shown in Figure 9 and Table 10; it is then divided by 1.98 to achieve the allowance strength. At 700 °C in the process of steady-state analysis, it can be found that in the range from $n = 3$ to $1/3$, although the maximum shear stress in the pipe is far lower than the yield strength and allowance stress, the maximum shear stress on the inner pipe wall contacting LBE is still generally higher than the yield strength. The maximum shear stress at other parts of the pipe shows a slight trend, as shown in Figure 10 and Table 11. Regarding corrosion resistance analysis, as shown in Figure 11 and Table 12, the linear distribution is slightly lower than 1.25 wt.%. The surface silicon concentration gradually increases with the rise of volume fraction levels. The silicon concentration distribution decreases as the volume fraction drops. Although increasing the volume fraction of two-phase functionally graded materials can effectively improve the silicon concentration and achieve corrosion resistance, there is a problem of excessive surface stress when in contact with LBE.

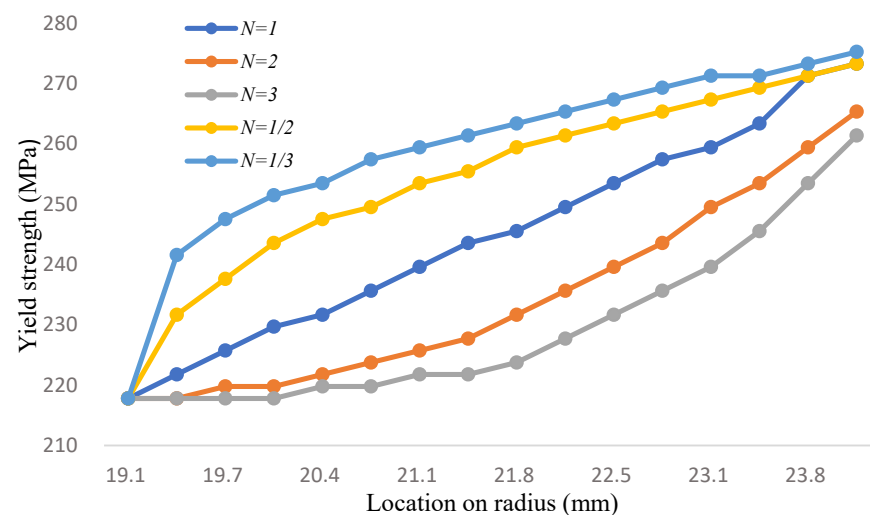
**Figure 9.** The yield strength of the two-phase model (Unit: MPa, Temp: 700 °C).

Table 10. The yield strength of the two-phase model (Unit: MPa, Temp: 700 °C).

Location (mm)	19.05	19.61	20.18	20.75	21.31	21.88	22.45	23.01	23.58	24.15
N = 1	218.00	222.00	226.00	230.00	240.00	246.00	249.00	253.00	263.00	273.00
N = 2	218.00	220.00	224.00	228.00	232.00	236.00	244.00	253.00	259.00	265.00
N = 3	218.00	220.00	222.00	224.00	224.00	226.00	242.00	248.00	256.00	264.00
N = 1/2	218.00	234.00	250.00	255.00	258.00	260.00	260.00	262.00	265.00	273.00
N = 1/3	218.00	242.00	251.00	257.00	259.00	261.00	265.00	267.00	269.00	275.00

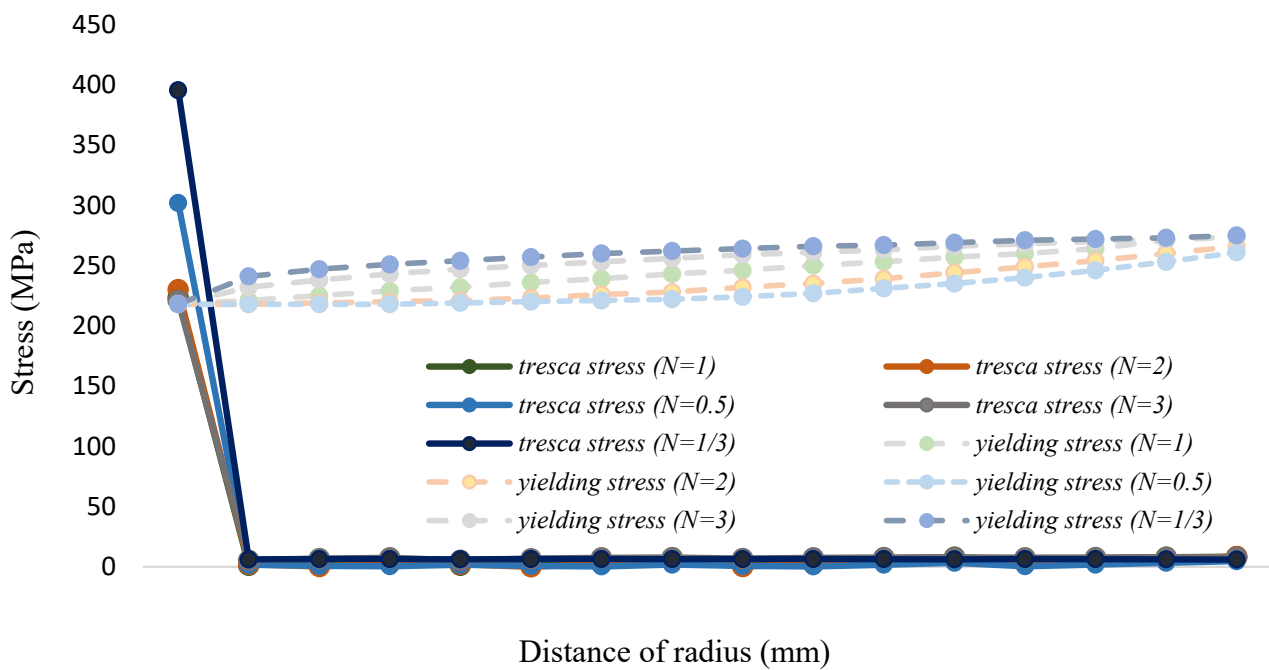


Figure 10. The Tresca stress and yield strength distribution (Fe-12Cr-2Si-T91, T = 700 °C).

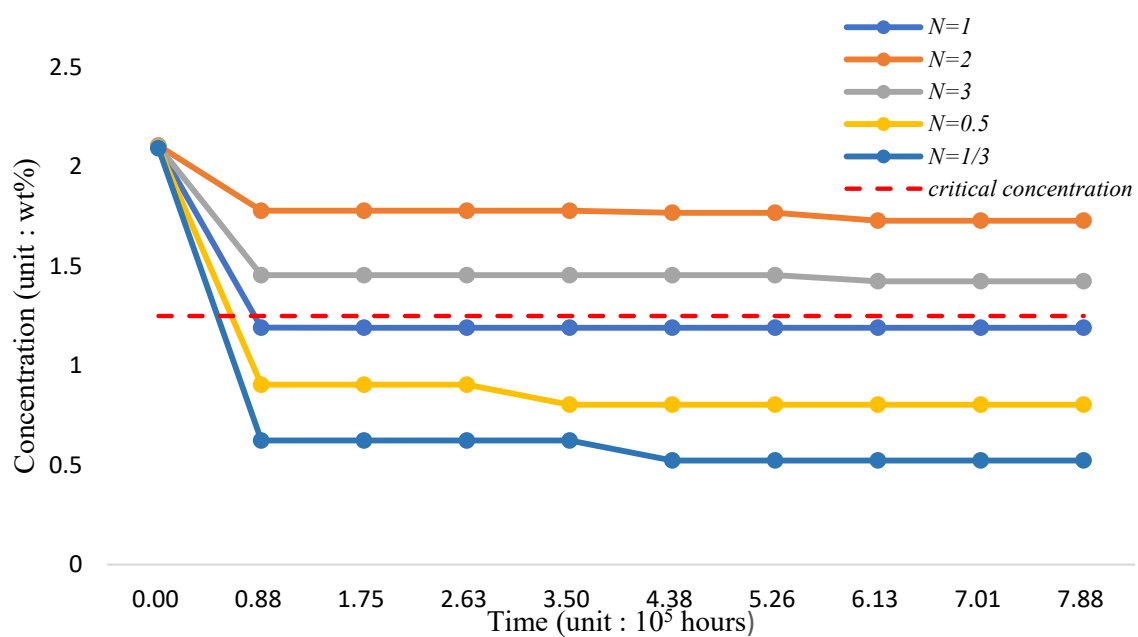


Figure 11. The silicon concentration of the two-phase model (Unit: wt.%, Temp: 700 °C).

Table 11. The Tresca stress and yield strength distribution (Fe-12Cr-2Si-T91, T = 700 °C).

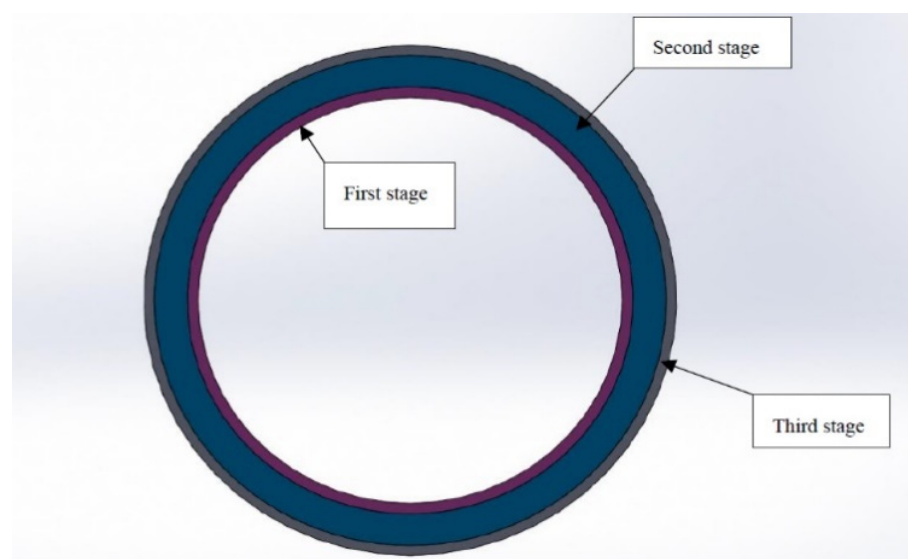
Location (mm)	19.05	19.61	20.18	20.75	21.31	21.88	22.45	23.01	23.58	24.15
N = 1	223.50	1.34	4.28	6.22	4.14	7.24	4.29	6.04	7.24	7.95
N = 2	230.00	2.16	2.11	2.97	4.72	5.14	2.65	7.02	5.13	8.45
N = 3	221.00	5.38	5.42	6.80	7.47	7.76	6.86	7.47	7.75	7.84
N = 1/2	302.00	1.68	7.65	1.83	1.73	3.36	1.83	3.36	4.72	4.72
N = 1/3	395.46	6.17	6.47	6.22	6.46	6.38	6.22	6.48	6.37	6.05

Table 12. The silicon concentration of the two-phase model (Unit: wt.%, Temp: 700 °C).

Time (10 ⁵ h)	0	0.876	1.752	2.628	3.504	4.38	5.25	6.132	7.00	7.88
N = 1	2.0997	1.1907	1.1907	1.1907	1.1907	1.1907	1.1907	1.1907	1.1907	1.1907
N = 3	2.1064	1.7885	1.7885	1.7885	1.7885	1.7885	1.7885	1.7885	1.7885	1.7885
N = 2	2.103	1.4847	1.4847	1.4847	1.4847	1.4847	1.4847	1.4847	1.4847	1.4847
N = 1/2	2.0964	0.9039	0.9039	0.9039	0.9039	0.9039	0.9039	0.9039	0.9039	0.9039
N = 1/3	2.0926	0.6236	0.6236	0.6236	0.6236	0.6236	0.6236	0.6236	0.6236	0.6236

4.3. Characterization of Structural for Three-Phase FGM Pipes (Fe-12Cr-2Si-TiO₂-T91)

TiO₂ has a lower diffusion coefficient and higher young's modulus than Fe-12Cr-2Si and T91 alloys. Therefore, changing the two-phase FGM to the three-phase Fe-12Cr-2Si-TiO₂-T91 model may yield better corrosion resistance and high strength. The structure of the three-phase functionally graded materials mainly improves the traditional circular tube structure through titanium dioxide, which has an oxygen level of 10% [42]. The structure of the three-phase FGM gradually transforms from the Fe12Cr2Si solid solution on the inner surface to TiO₂. The process is to apply the volume fraction method of Equations (2)–(10) to the calculation of material mechanical properties. It converts from 100% Fe-12Cr-2Si to 50% Fe-12Cr-2Si and 50% TiO₂, then to 100% TiO₂, gradually to 90% TiO₂ and 10% T91 on the outer diameter; The process is shown in Figure 12. The material structure from the inner wall to the outer wall is divided into three stages. The first stage is the radius from 19.05 to 20.06 mm, the second stage is 20.06–23.86 mm, and the third stage is 23.86–24.15 mm.

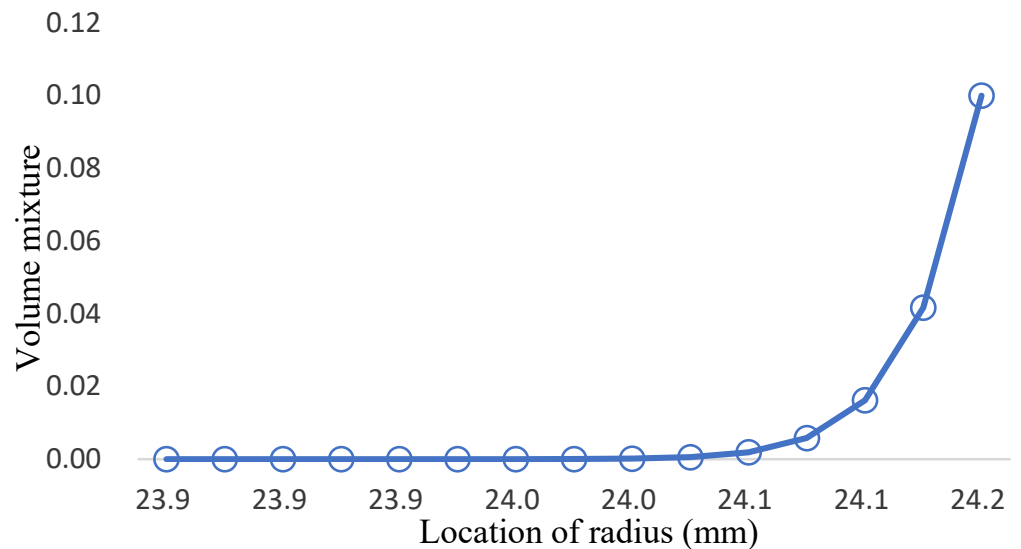
**Figure 12.** Three-phase model distribution of coolant pipe (Fe-12Cr-2Si-TiO₂-T91).

The Fe-12Cr-2Si-TiO₂-T91 three-phase structure considers the mechanical value of material strength, such as the gradual increase of young’s modulus strength, which can convert the stress of the contact surface between the inner side and LBE. The Fe-12Cr-2Si-TiO₂-T91 three-phase structure also considers that the diffusion coefficient rapidly reduces and distributes with the geometric inner diameter of the pipe to the outer diameter, which effectively inhibits the rapid diffusion of silicon concentration. The initial silicon concentration distribution of the FGM structure varies gradually compared to that of the traditional FGC, which avoids the loss of silicon concentration and extends the working life. In conclusion, the Fe-12Cr-2Si-TiO₂-T91 three-phase model should improve the strength and high-temperature corrosion resistance of the FGC and two-phase structure.

Considering Young’s modulus and the yield strength of T91 being lower when the temperature rises, the ratio of TiO₂ should increase when it is close to the inner wall for better strength; the low diffusion coefficient can also improve the resistance of Fe-12Cr-2Si. The analysis process divides the three-phase structure into three stages. The first stage converts from 100% Fe-12Cr-2Si to 50% Fe-12Cr-2Si and 50% TiO₂; the second stage converts from 50% Fe-12Cr-2Si and 50% TiO₂ to 100% TiO₂; and the third stage converts from 100% TiO₂ to 90% TiO₂ and 10% T91. The change of the volume fraction value is only for the first and second stages, and the volume fraction value in the third stage remains $n = 12$, which is shown in Figure 13a and Table 13. In this research, there are four groups with different volume mixtures in the three-phase model, which are (1,1,12), (2,1,12), (6,4,12), and (10,8,12), the distributions of volume mixture are shown in Figure 13b,c, and Tables 14 and 15, respectively.

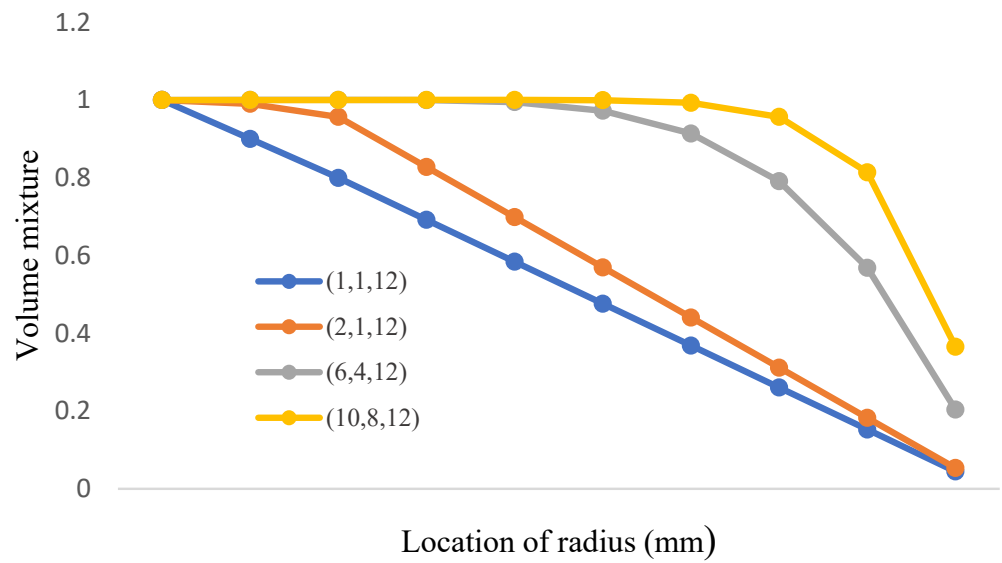
Table 13. The volume mixture of T91 for three-phase FGM.

Location (mm)	23.86	23.88	23.92	23.96	23.98	24.00	24.04	24.06	24.10	24.15
Volume of mixture	0.00	0.00	0.00	0.00	2.92×10^{-5}	1.39×10^{-4}	5.52×10^{-4}	1.62×10^{-2}	4.16×10^{-2}	0.1

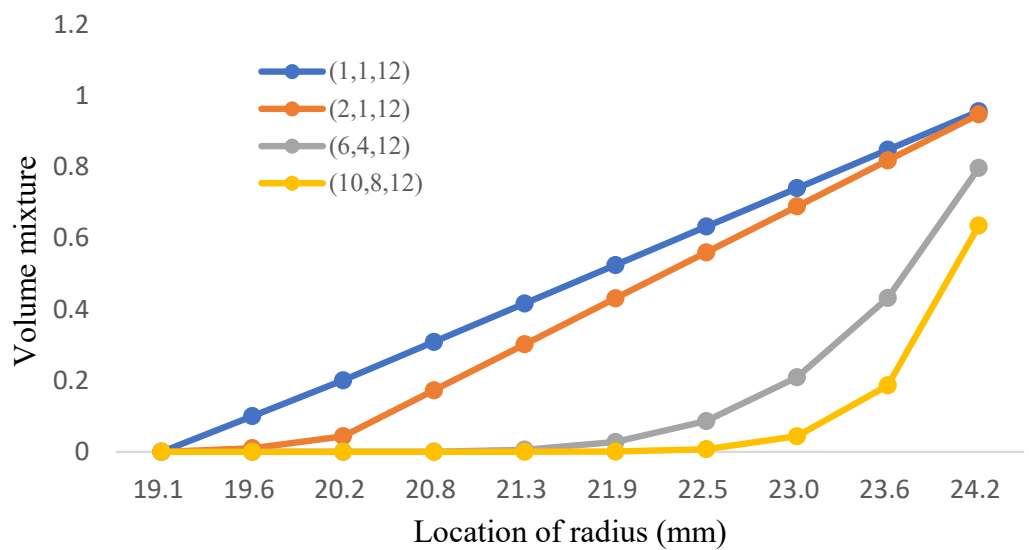


(a)

Figure 13. Cont.



(b)



(c)

Figure 13. (a). the volume mixture of T91 for three-phase FGM; (b). the volume mixture of Fe-12Cr-2Si for three-phase FGM; (c). the volume mixture of TiO₂ for three-phase FGM.

Table 14. The volume mixture of Fe12Cr2Si for three-phase FGM.

Location (mm)	19.05	19.57	20.08	20.59	21.10	21.61	22.12	22.63	23.14	23.86
(1,1,12)	1.00	0.89	0.79	0.69	0.58	0.47	0.36	0.26	0.15	0.04
(2,1,12)	1.00	0.98	0.95	0.82	0.69	0.56	0.44	0.31	0.18	0.05
(6,4,12)	1.00	0.99	0.98	0.98	0.98	0.97	0.91	0.79	0.56	0.20
(10,8,12)	1.00	1.00	1.00	1.00	0.99	0.98	0.98	0.95	0.81	0.36

Table 15. The volume mixture of TiO₂ for three-phase FGM.

Location (mm)	19.05	19.61	20.18	20.75	21.31	21.88	22.45	23.01	23.58	24.15
(1,1,12)	0.00	0.1002	0.2006	0.3084	0.4163	0.5242	0.6320	0.7399	0.8477	0.9556
(2,1,12)	0.00	0.1004	0.0436	0.1726	0.3017	0.4307	0.5597	0.6888	0.8178	0.9469
(6,4,12)	0.00	1.01×10^{-6}	5.74×10^{-5}	4.36×10^{-4}	5.67×10^{-3}	0.02774	0.0864	0.2093	0.4317	0.7967
(10,8,12)	0.00	1.02×10^{-10}	8.54×10^{-8}	2.29×10^{-7}	3.16×10^{-5}	7.67×10^{-4}	7.67×10^{-4}	0.0437	0.1863	0.6348

According to the calculation method of volume fraction of yield strength in Equation (33), the yield strength distribution of the Fe-12Cr-2Si-TiO₂-T91 three-phase FGM at different temperatures is shown in Figures 14–16 and Tables 16–18, respectively. The Tresca stress analysis from Figures 17–19 and Tables 19–21, with the increase of volume fraction, the distribution of maximum shear stress value decreases accordingly. When the volume fraction values of the first and second stages are 10 and 8, respectively, the maximum shear stress value reduces to less than the allowance stress. That is, less than almost half of the yield strength; that is, the combination of (10,8,12) can achieve this result.

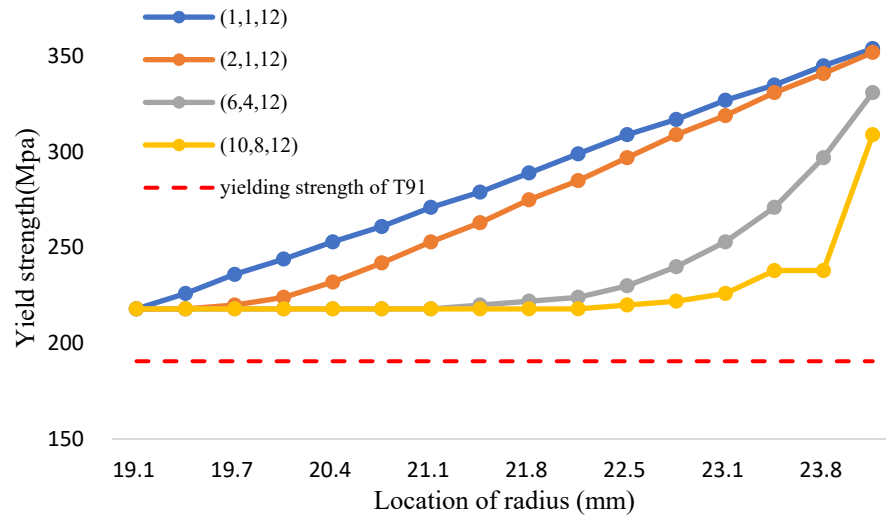


Figure 14. The yield strength of FGM and T91 alloys (Fe-12Cr-2Si-TiO₂-T91, Temperature: 700 °C).

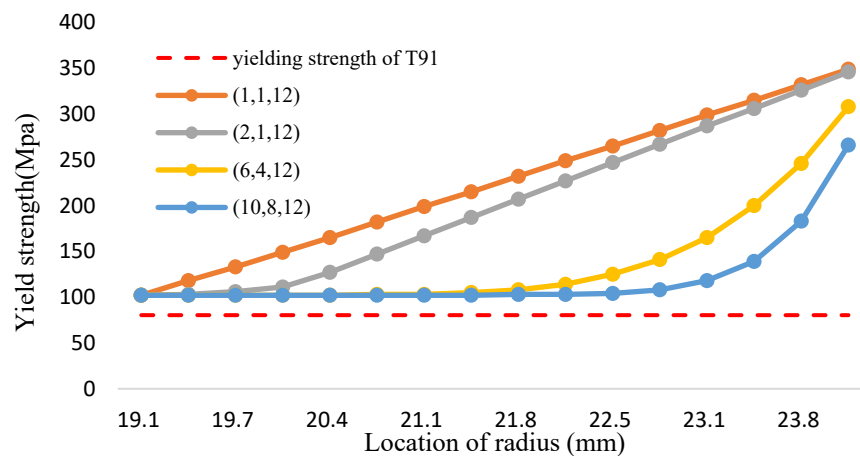


Figure 15. The yield strength of FGM and T91 alloys (Fe-12Cr-2Si-TiO₂-T91, Temperature: 1000 °C).

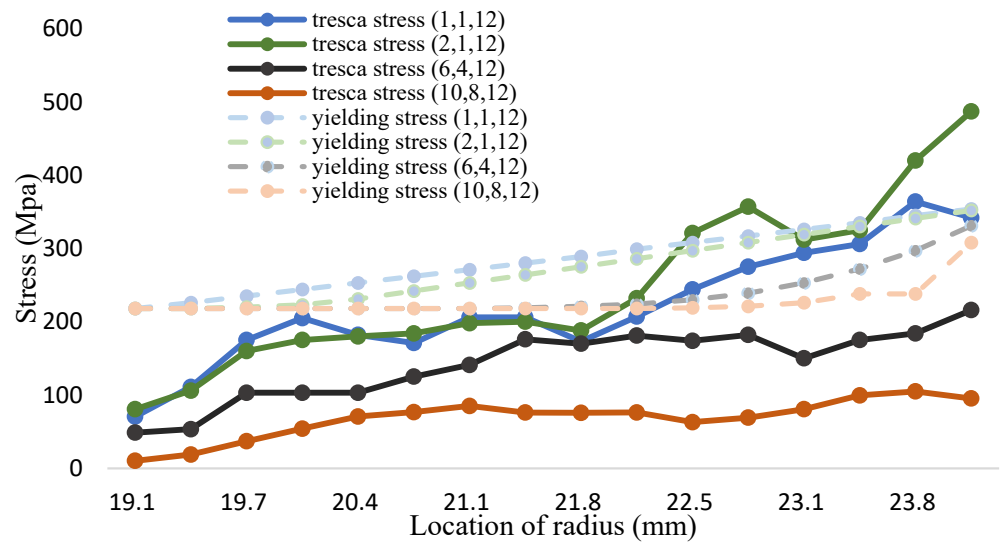


Figure 17. The tresca stress and yield strength (Fe-12Cr-2Si-TiO₂-T91, Unit: Mpa, Temperature: 700 °C).

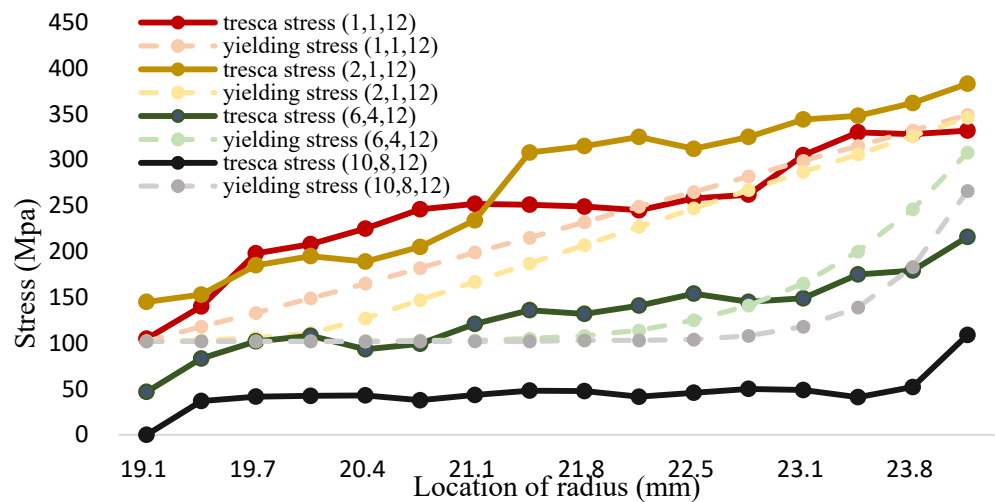


Figure 18. The tresca stress and yield strength (Fe-12Cr-2Si-TiO₂-T91, Unit: Mpa, Temperature: 1000 °C).

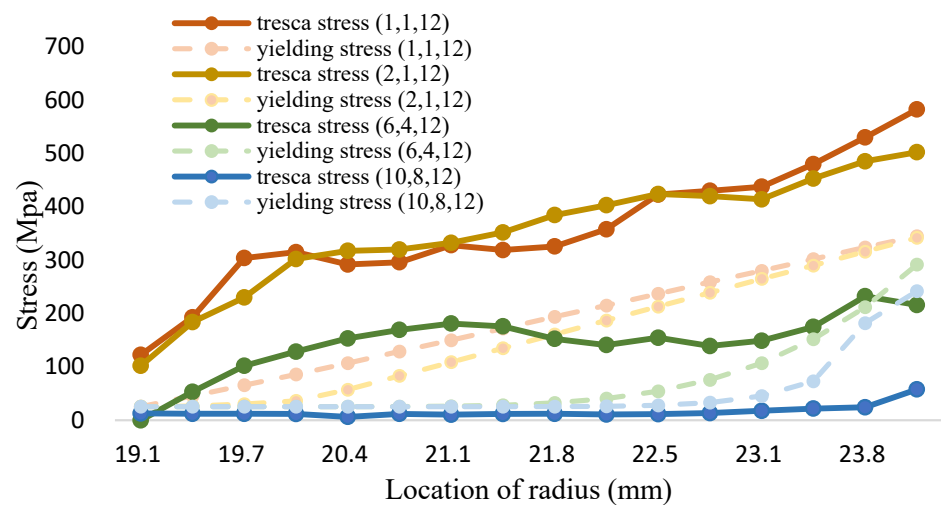


Figure 19. The tresca stress and yield strength (Fe-12Cr-2Si-TiO₂-T91, Unit: Mpa, Temperature: 1200 °C).

Table 19. The tresca stress and yield strength (Fe-12Cr-2Si-TiO₂-T91, Unit: Mpa, Temp: 700 °C).

Location (mm)	19.05	19.61	20.18	20.75	21.31	21.88	22.45	23.01	23.58	24.15
(1,1,12)	70.58	111.00	175.00	171.00	244.00	275.00	294.00	306.00	364.00	342.00
(2,1,12)	80.57	106.00	160.00	180.00	198.00	188.00	232.00	357.00	325.00	487.00
(6,4,12)	48.70	53.30	103.00	125.00	141.00	170.00	181.00	174.00	182.00	216.00
(10,8,12)	10.21	18.70	36.80	76.60	85.00	76.00	75.70	76.20	69.10	95.20

Table 20. The tresca stress and yield strength (Fe-12Cr-2Si-TiO₂-T91, Unit: Mpa, Temp: 1000 °C).

Location (mm)	19.05	19.61	20.18	20.75	21.31	21.88	22.45	23.01	23.58	24.15
(1,1,12)	105.00	198.00	225.00	252.00	245.00	258.00	262.00	305.00	330.00	332.00
(2,1,12)	145.00	153.00	185.00	195.00	234.00	308.00	315.00	325.00	348.00	383.00
(6,4,12)	46.90	102.00	93.30	99.30	136.00	132.00	141.00	154.00	175.00	216.00
(10,8,12)	0.00	36.90	41.70	37.70	43.50	48.20	41.60	45.90	52.10	109.00

Table 21. The tresca stress and yield strength (Fe-12Cr-2Si-TiO₂-T91, Unit: Mpa, Temperature: 1200 °C).

Location (mm)	19.05	19.61	20.18	20.75	21.31	21.88	22.45	23.01	23.58	24.15
(1,1,12)	122.49	292.00	319.00	326.00	358.00	423.00	430.00	438.00	480.00	583.00
(2,1,12)	102.01	230.00	302.00	333.00	352.00	385.00	403.00	414.00	485.00	502.00
(6,4,12)	0.00	53.30	129.00	169.00	176.00	153.00	155.00	139.00	175.00	216.00
(10,8,12)	12.79	12.10	12.10	11.90	11.90	10.60	12.20	13.40	24.30	58.00

The silicon concentration on the surface of three-phase FGM structure pipe wall in 700 °C working environment is shown in Figure 20 and Table 22. Based on the analysis results, the addition of TiO₂ and the decrease of the proportion of T91 material can effectively improve the maintenance of surface silicon concentration. If the volume fraction of Fe-12Cr-2Si-TiO₂-T91 is maintained at (10,8,12), the silicon concentration can approach 2.0384 wt.%; it can significantly improve the corrosion resistance compared with the FGC structure.

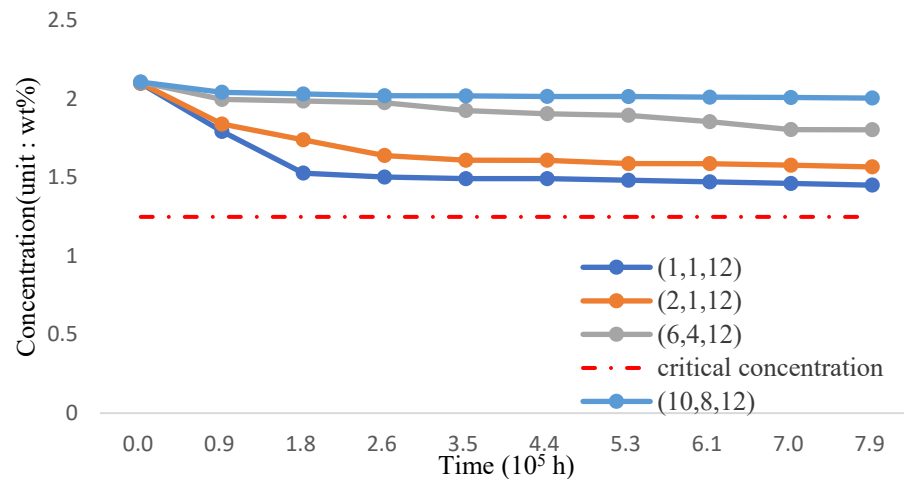


Figure 20. The silicon concentration (Fe-12Cr-2Si-TiO₂-T91, Temperature: 700 °C).

Table 22. The silicon concentration (Fe-12Cr-2Si-TiO₂-T91, Temperature: 700 °C, Unit: wt.%).

Time (10 ⁵ h)	0	0.876	1.752	2.628	3.504	4.38	5.25	6.132	7.00	7.88
(1,1,12)	2.0988	1.7930	1.7928	1.7925	1.7923	1.7921	1.7919	1.7917	1.7916	1.7914
(2,1,12)	2.1005	1.8397	1.8397	1.8396	1.8395	1.8392	1.8389	1.8381	1.8376	1.8373
(6,4,12)	2.1060	1.9965	1.9963	1.9958	1.9953	1.9950	1.9947	1.9943	1.9941	1.9937
(10,8,12)	2.1076	2.0419	2.0414	2.0399	2.0397	2.0392	2.0389	2.0388	2.0385	2.0384

The maximum shear stress value of 1000 °C is shown in Figure 18 and Table 20. It can be seen from the figure that the tresca stress distribution of Fe-12Cr-2Si and TiO₂ presents a linear distribution for the (1,1,12). The stress is higher than yield strength. However, the distribution of the maximum shear stress value decreases with the increment of the volume fraction value. When the volume fraction values of Fe-12Cr-2Si and TiO₂ are 10 and 8 respectively, the maximum shear stress can also be reduced to less than the allowable stress, that is, less than half of the yield strength. The results are consistent with those in the environment of 700 °C. When the volume integration rate increases, the maximum shear stress can be effectively reduced.

The variation of silicon concentration on the surface of three-phase functionally graded material structure pipe wall in 1000 °C working environment is shown in Figure 21 and Table 23. From the analysis results, the incorporation of TiO₂ and reducing the proportion of T91 material can still effectively improve the maintenance of surface silicon concentration. If the volume mixture of Fe-12Cr-2Si-TiO₂-T91 is maintained (10,8,12), the silicon concentration can approach 1.9906 wt.%.

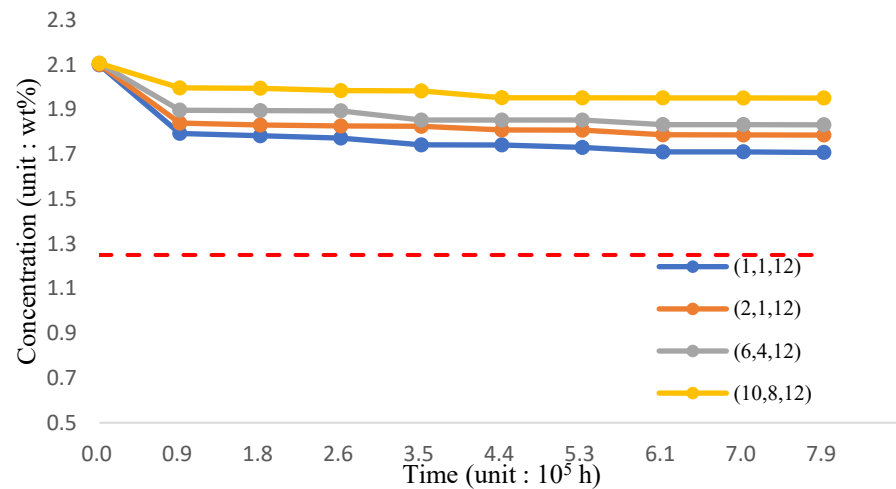


Figure 21. The silicon concentration (Fe-12Cr-2Si-TiO₂-T91, Temperature: 1000 °C).

Table 23. The silicon concentration (Fe-12Cr-2Si-TiO₂-T91, Temperature: 1000 °C, Unit: wt.%).

Time (10 ⁵ h)	0	0.876	1.752	2.628	3.504	4.38	5.25	6.132	7.00	7.88
(1,1,12)	2.0988	1.7927	1.7923	1.7160	1.7912	1.7909	1.7905	1.7902	1.78991	1.7896
(2,1,12)	2.1005	1.8387	1.8391	1.8389	1.8383	1.8381	1.8372	1.8365	1.8358	1.8356
(6,4,12)	2.1060	1.9962	1.9944	1.9934	1.9924	1.9923	1.9921	1.9919	1.9918	1.9910
(10,8,12)	2.1060	1.9960	1.9944	1.9940	1.9919	1.9916	1.9913	1.9910	1.9908	1.9906

The maximum shear stress value of 1200 °C is shown in Figure 19 and Table 21. It can be seen from the figure that the distribution of Fe-12Cr-2Si and TiO₂ presents a linear

distribution state for (1,1,12). However, the distribution of the maximum shear stress value decreases as the volume fraction increases. When the volume fraction values of Fe-12Cr-2Si and TiO₂ are 10 and 8, respectively, the maximum shear stress value can also be reduced to less than the yield strength and allowable strength.

The variation of silicon concentration on the surface of the three-phase FGM pipe wall in the 1200 °C-working environment is shown in Figure 22 and Table 24. Per the analysis results, incorporating TiO₂ and reducing the proportion of T91 material can still effectively improve the maintenance of surface silicon concentration. If the proportion of the Fe-12Cr-2Si-TiO₂-T91 body integral rate is maintained (10,8,12) for 8.8×10^5 h, the silicon concentration can approach 2.0190 wt.% stably.

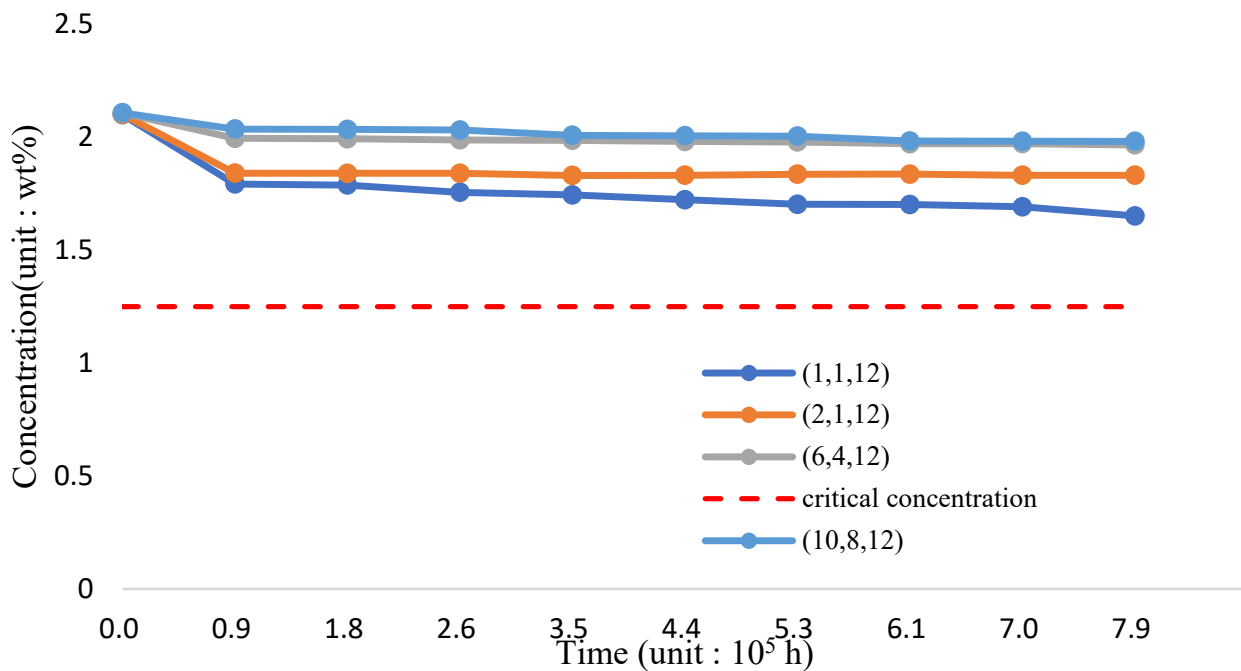


Figure 22. The silicon concentration (Fe-12Cr-2Si-TiO₂-T91, Temperature: 1200 °C).

Table 24. The silicon concentration (Fe-12Cr-2Si-TiO₂-T91, Temperature: 1200 °C, Unit: wt.%).

Time (10 ⁵ h)	0	0.876	1.752	2.628	3.504	4.38	5.25	6.132	7.00	7.88
(1,1,12)	2.0988	1.7927	1.7823	1.7860	1.7812	1.7809	1.7805	1.7802	1.78991	1.7896
(2,1,12)	2.1005	1.8387	1.8391	1.8389	1.8383	1.8381	1.8372	1.8365	1.8358	1.8356
(6,4,12)	2.1060	1.9940	1.9920	1.9870	1.9850	1.9810	1.9780	1.9770	1.9760	1.9760
(10,8,12)	2.1060	2.0350	2.0340	2.0310	2.0270	2.0260	2.0240	2.0220	2.0210	2.0190

From the Figures 17–19, it can be clearly seen that all the volume mixture model (10,8,12) can reach the Tresca stress is lower than the yield strength and the allowance strength at different temperature. The margin of safety in this research can be evaluated by Equation (13), the allowable strength is the tresca stress from the volume mixture (10,8,12). These distributions can be depicted in the Figure 23 and Table 25, from the 700 to 1000 °C the safety margin of inner wall is much higher than other place because the Tresca stress closing to the inner wall is very small. When the temperature is higher, both the Fe-12Cr-2Si and T91 alloy have a lower yield strength. It makes the safety margin of 1200 °C reduced in front of the inner wall of coolant pipes. However, thanks to the high yield strength of titanium dioxide, the safety margin closed to the outer wall increases gradually.

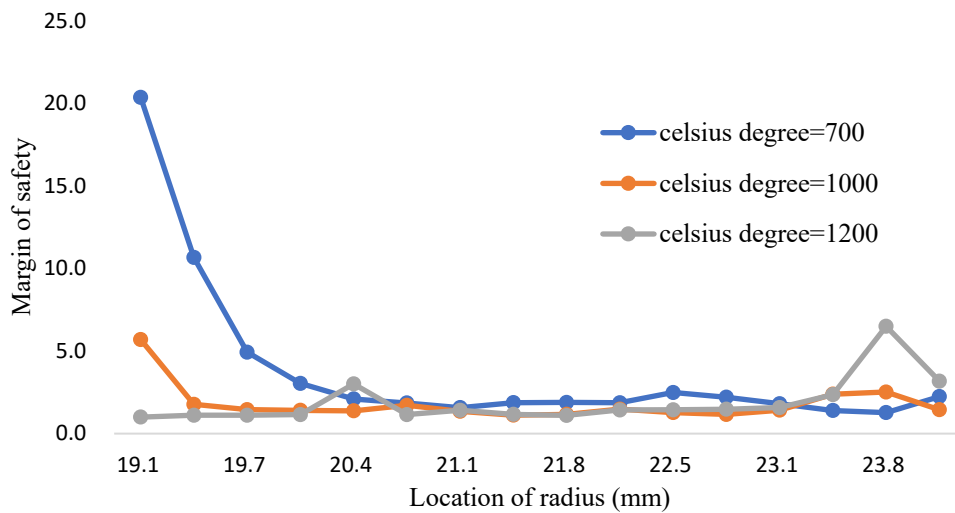


Figure 23. The margin of safety for three-phase model (Fe-12Cr-2Si-TiO₂-T91, volume of mixture: (10,8,12)).

Table 25. The margin of safety for three-phase model (Fe-12Cr-2Si-TiO₂-T91, volume of mixture: (10,8,12)).

	19.05	19.61	20.18	20.75	21.31	21.88	22.45	23.01	23.58	24.15
700 °C	20.35	10.66	3.04	2.09	1.56	1.87	1.88	2.48	1.39	2.24
1000 °C	5.69	1.76	1.40	1.71	1.34	1.12	1.16	1.27	2.38	1.44
1200 °C	0.99	1.11	1.14	3.00	1.41	1.16	1.43	1.47	1.57	3.17

The margin of safety calculated in a high temperature environment can be an evaluation for LBLOCA condition [14]. The variation of temperature for this incident is range from 25 to 1200 °C. In this study, the results of margin safety is about 0.99~20.35, there is a high improvement for the safety of coolant pipe and cladding construction compared with the margin safety about 76~98% in Section 3.1. Therefore, the three-phase FGM model can be an optimized design for the coolant pipe structure in consider of corrosion resistance and safety evaluation.

5. Conclusions

The two-phase and three-phase functionally graded material structures have improved the LBE static hydraulic erosion and corrosion resistance of the existing FGC welding structure in a high-temperature environment. The traditional FGC welding structure is a Fe-12Cr-2Si-T91 two-layer composite material. The two-phase FGM changes the FGC two-layer structure to the progressive Fe-12Cr-2Si-T91 FGM structure, which gradually changes from the surface Fe-12Cr-2Si to T91 alloys. The three-phase structure Fe-12Cr-2Si-TiO₂-T91 combines the two-phase FGM and TiO₂ materials to strengthen the structural strength and improve corrosion resistance to high temperatures. The simulation results under different high-temperature environments can be summarized as follows.

- (1) The results show that under the corrosion boundary of steady-state LBE coolant, the tresca stress of the FGC structure in a high-temperature environment is much higher than the allowance stress, and the overall structure has safety concerns regarding entering plastic deformation. If the surface silicon concentration is higher than 1000 °C, as it drops below 1.25 wt.% within ten years, the Fe-12Cr-2Si coating on the substrate surface needs to be replaced.
- (2) The design of the two-phase FGM has been applied to the design of nuclear reactor pipes and solar cell structures [23,43]. In this study, the tresca stress of coolant pipes is preliminarily analyzed with the two-phase FGM Fe-12Cr-2Si-T91. When it changes from linear to nonlinear distribution with the increase of volume fraction, it does

- effectively improve the surface silicon concentration. Therefore, Fe-12Cr-2Si with high silicon concentration can have sufficient time to maintain a concentration higher than 1.25 wt.% on the surface in contact with LBE; However, the maximum shear stress at the contact surface with LBE is still greater than the yield strength.
- (3) This study further adopts the structure of the three-phase model Fe-12Cr-2Si-TiO₂-T91 to strengthen the system's function and improve the reliability of the results. The analysis results show that the maximum shear stress distribution under a high-temperature environment can be lower than the yield strength divided by 1.98-lower than the allowable stress. Meanwhile, the silicon concentration can still be maintained above 1.25 wt.% within 100 years. It can be confirmed that the intervention of TiO₂ can optimize the structural strength and corrosion resistance of FGM. However, the proportion of T91 in the model must be effectively reduced to prevent strength reduction when the temperature is very high. The results show that when the volume fraction of Fe-12Cr-2Si-TiO₂-T91 reaches (10,8,12), the silicon concentration can be maintained above 1.900 wt.%, reaching a stable situation, so that there are enough silicon elements on its surface to react with LBE, forming an oxide layer to further resist the corrosion of LBE. In this research, the Fe-12Cr-2Si-TiO₂-T91 model can extend the life of corrosive resistance more 60 years compared with the traditional FGC structure.
 - (4) In this research, when the volume fraction value is (10,8,12) for the three-phase model, it can effectively reduce the maximum shear stress and silicon concentration diffusion process under different temperature distributions in the existing nuclear reactor. Therefore, the development of FGM cannot be limited to the two-phase functional structure. The three-phase FGM model can be a structural optimization method in the future for the design of nuclear reactor parts and other physical high load products.

Author Contributions: Writing—original draft, K.-C.L.; Writing—review & editing, H.-Y.L. All authors have read and agreed to the published version of the manuscript.

Funding: This research received no external funding.

Institutional Review Board Statement: Not applicable.

Informed Consent Statement: Not applicable.

Data Availability Statement: Data is contained within the article.

Conflicts of Interest: The authors declare no conflict of interest.

References

1. Sheng, G.G.; Wang, X. Thermomechanical vibration analysis of a functionally graded shell with flowing fluid. *Eur. J. Mech. A Solids* **2008**, *27*, 1075–1087. [[CrossRef](#)]
2. Hui, S.S. Thermal postbuckling behavior of functionally graded cylindrical shells with temperature-dependent properties. *Int. J. Solids Struct.* **2004**, *41*, 1961–1974.
3. Hui, S.S. Thermal postbuckling of shear deformable FGM cylindrical shells surrounded by an elastic medium. *J. Eng. Mech.* **2013**, *139*, 979–991. [[CrossRef](#)]
4. Kyung, S.N.; Kim, J.H. Three-dimensional thermomechanical buckling analysis for functionally graded composite plates. *Comp. Struct.* **2006**, *73*, 413–422.
5. Reddy, J.N.; Chin, C.D. Thermomechanical analysis of functionally graded cylinders and plates. *J. Therm. Stress.* **1998**, *21*, 593–626. [[CrossRef](#)]
6. Wenxuan, X.; Yongwei, W.; Xunfeng, L. Experimental investigation of the thermal hydraulics in lead bismuth eu-tectic-helium experimental loop of an accelerator-driven system. *Nucl. Eng. Technol.* **2016**, *48*, 1154–1161.
7. Ballinger, R.G. *The Development and Production of a Functionally Graded Composite for Pb-Bi Service*; Technical Report DOE-ID1 4742; U.S. Department of Energy Office of Scientific and Technical Information: Oak Ridge, TN, USA, 2011.
8. Elliott, S.F. Materials Testing and Development of Functionally Graded Composite Fuel Cladding and Piping for the Lead-Bismuth Cooled Nuclear Reactor. Master's Thesis, Massachusetts Institute of Technology, Cambridge, MA, USA, 2013.
9. Serrano De Caro, M.; Woloshun, K.A.; Rubio, F.V.; Maloy, S.A. *Materials Selection for the Lead-Bismuth Corrosion and Erosion Tests in DELTA Loop*; Technical Report LA-UR-13-22282; Los Alamos National Laboratory: Los Alamos, NM, USA, 2013.
10. Joonho, M.; Sungyu, K.; Won, D.P. Initial oxidation behavior of Fe-Cr-Si alloys in 1200 °C steam. *J. Nucl. Mater.* **2019**, *513*, 297–308.

11. Woo, Y.J.; Sung, C.H. Analysis of functionally graded material plates using sigmoidal law. *Math. Probl. Eng.* **2017**, *4*, 363–374.
12. Jeongyoun, L. Effects of Chromium and Silicon on Corrosion of Iron Alloys in Lead-Bismuth Eutectic. Ph.D. Thesis, Massachusetts Institute of Technology, Cambridge, MA, USA, 2006.
13. Wang, H.; Xiao, J.; Wang, H.; Chen, Y.; Yin, X.; Guo, N. Corrosion behavior and surface treatment of cladding materials used in high-temperature lead-bismuth eutectic alloy: A review. *Coatings* **2021**, *11*, 364. [[CrossRef](#)]
14. Ahn, K.; Joo, K.; Park, S.-P. Safety evaluation of silicon carbide and zircaloy-4 cladding during a large-break loss-of-coolant accident. *Energies* **2018**, *11*, 3324. [[CrossRef](#)]
15. Ting, W.L. Risk-Informed Safety Margin Characterization for a Larger Break Loss-of-Coolant Accident of Nuclear Power Plants and Associated Peak Cladding Temperature Margin Evolution. Master's Thesis, University of Liverpool, Liverpool, UK, 2019.
16. Masahide, S.; Kenta, M.; Takashi, S. Verification of safety margin of reactor pressure vessel exposed to various thermal transients based on probabilistic approach. *E-J. Adv. Maint.* **2020**, *11*, 172–178.
17. Vincenzo, V.R.; Thierry, W. The high burn-up structure in nuclear fuel. *Mater. Today* **2010**, *13*, 24–32.
18. Short, M.P.; Ballinger, R.G.; Hanninen, H.E. Corrosion resistance of alloys F91 and Fe-12Cr-2Si in lead-bismuth eutectic up to 715 °C. *J. Nucl. Mater.* **2013**, *434*, 259–281. [[CrossRef](#)]
19. Cairang, W.; Ma, S.; Gong, X.; Zeng, Y.; Yang, H.; Xue, D.; Qin, Y.; Ding, X.; Sun, J. Oxidation mechanism of refractory Molybdenum exposed to oxygen-saturated lead-bismuth eutectic at 600 °C. *Corros. Sci.* **2020**, *179*, 109132. [[CrossRef](#)]
20. Short, M.P.; McAlpine, S.; Tonks, M.; Rezwani, A.; Zhang, J.; Leong, A.; Xie, Y.; Rausch, J.; Salkin, J.; Bachav, M.; et al. *NEUP Final Report: Multilayer Composite Fuel Cladding and Core Internals for LWR Performance Enhancement and Severe Accident Tolerance*; Massachusetts Institute of Technology: Cambridge, MA, USA, 2019. [[CrossRef](#)]
21. Libardi, J.; Grigorov, K.G.; Massi, M. Diffusion of silicon in titanium dioxide thin films with different degree of crystallinity: Efficiency of TiO₂ and tin barrier layers. *Vacuum* **2016**, *128*, 178–185. [[CrossRef](#)]
22. Manjubala, I. Effect of TiO₂-Ag₂O additives on the formation of calcium phosphate based functionally graded bioceramics. *Biomaterials* **2000**, *21*, 1995–2002. [[CrossRef](#)]
23. Kim, H.G.; Kim, H.I.; Jung, Y.I. Development of surface modified Zr Cladding by Coating Technology for ATF. In Proceedings of the Top Fuel 2016: LWR Fuels with Enhanced Safety and Performance, Boise, ID, USA, 11–15 September 2016.
24. Zhang, C.; Chen, F.; Huang, Z.; Jia, M.; Chen, G.; Ye, Y.; Lin, Y.; Liu, W.; Chen, B.; Shen, Q.; et al. Additive manufacturing of functionally graded materials: A review. *Mater. Sci. Eng. A* **2019**, *764*, 138209. [[CrossRef](#)]
25. Zhang, H.; Liu, S.; Han, S. The numerical manifold method for transient moisture diffusion in 2D functionally graded materials. *IOP Conf. Ser. Earth Environ. Sci.* **2018**, *189*, 032017. [[CrossRef](#)]
26. Zhang, H.; Liu, S.; Han, S. Modelling steady moisture diffusion in functionally graded materials with the numerical manifold method. *IOP Conf. Ser. Earth Environ. Sci.* **2018**, *189*, 042018. [[CrossRef](#)]
27. Zhou, B. The Effect of the Pre-Existing Surface Crack Morphologies on the Thermal Fracture of Ceramic Coatings. Ph.D. Thesis, Purdue University, West Lafayette, IN, USA, 2003.
28. Cho, J.R.; Ha, D.Y. Averaging and finite element discretization approaches in the numerical analysis of functionally graded materials. *Mater. Sci. Eng.* **2001**, *302*, 187–196. [[CrossRef](#)]
29. Wang, J. Study of Microstructure Evolution in F/M steel T91 by In-Situ Synchrotron Wide-Angle X-rays Scattering. Master's Thesis, University of Illinois at Urbana, Champaign, IL, USA, 2017.
30. Raju, S.; Haraprasanna, T.; Arun, K.R. Thermal expansion characteristics of Fe-9Cr-0.12C-0.56Mn-0.24V-1.38W-0.06Ta (wt.%) reduced activation ferritic-martensitic steel. *J. Nucl. Mater.* **2015**, *459*, 150–158.
31. Wan, T.; Naoe, T.; Kogawa, H.; Futakawa, M.; Obayashi, H.; Sasa, T. Numerical study on the potential of cavitation damage in a lead-bismuth eutectic spallation target. *Materials* **2019**, *12*, 681. [[CrossRef](#)] [[PubMed](#)]
32. Titanium Dioxide—Titania (TiO₂). 2002. Available online: <https://www.azom.com/article.aspx?ArticleID=1179> (accessed on 2 November 2021).
33. Hosemann, P.; Kabra, S.; Stergar, E. Micro-structural characterization of laboratory heats of the Ferritic/Martensitic steels HT-9 and T91. *J. Nucl. Mater.* **2010**, *403*, 7–14. [[CrossRef](#)]
34. Beaulieu, R.A. *Margin of Safety Definition and Examples Used in Safety Basis Documents and the USQ Process*; Technical Report DOE/NV/25946-1891; Nevada Test Site: Mercury, NV, USA, 2013.
35. Li, B.; Liao, Q.; Zhang, H.; Shen, T.; Ge, F.; Daghbouj, N. The effects of stress on corrosion behavior of SIMP martensitic steel in static liquid lead-bismuth eutectic. *Corros. Sci.* **2021**, *187*, 109477. [[CrossRef](#)]
36. Wan, T.; Saito, S. Flow-Accelerated Corrosion of Type 316L Stainless Steel Caused by Turbulent Lead-Bismuth Eutectic Flow. *Metals* **2018**, *8*, 627. [[CrossRef](#)]
37. Postlethwaite, J.; Nestic, S. Hydrodynamics of disturbed flow and erosion-corrosion. Part I—single-phase flow study. *Can. J. Chem. Eng.* **1991**, *69*, 698–703.
38. Tamura, I.; Tomota, Y.; Ozawa, H. Strength and ductility of Fe-Ni-C alloys composed of austenite and martensite with various strength. *Camb. Inst. Met.* **1973**, *1*, 611–615.
39. Vasavi, B.; Raghavendra, G.; Shakuntla, O. State of the art in functionally graded materials. *Compos. Struct.* **2021**, *262*, 113596.
40. Samel, M.A. *Kinetics of Materials*; John Wiley & Sons: Hoboken, NJ, USA, 2005.
41. Wenyi, D.; Zhizhong, J.; Jingping, X. Interactions between alloy elements and oxygen at the steel-liquid LBE interface determined from first-principles molecular dynamics simulations. *Phys. Chem. Chem. Phys.* **2019**, *21*, 25521–25926. [[CrossRef](#)]

42. Eriko, Y.; Minoru, T. Corrosion resistance of Fe-Al-alloy-coated ferritic/martensitic steel under bending stress in high-temperature lead-bismuth eutectic. *J. Nucl. Sci. Technol.* **2012**, *48*, 797–804.
43. Tan, W.C.; Saw, L.H.; Yusof, F.; Thiam, H.S.; Xuan, J. Investigation of functionally graded metal foam thermal management system for solar cell. *Int. J. Energy Res.* **2019**, *44*, 9333–9349. [[CrossRef](#)]